学 位 論 文

# Electronic structure of 3*d* transition-metal compounds with competing *d*-*d* Coulomb interaction and *d*-ligand hybridization

# 強い*d*電子間クーロン相互作用と軌道混成の競合する3*d*遷移金属化合物の電子状態

澤 川 貴 司

学位論文

# Electronic structure of 3*d* transition-metal compounds with competing *d*-*d* Coulomb interaction and *d*-ligand hybridization

# 強い *d* 電子間クーロン相互作用と軌道混成の競合する 3*d* 遷移金属化合物の電子状態

溝川貴司

論文の内容の要旨

論文題目　Electronic structure of 3*d* transition-metal compounds with competing *d*-*d* Coulomb interaction and *d*-ligand hybridization

強い *d* 電子間クーロン相互作用と軌道混成の競合する
3*d* 遷移金属化合物の電子状態

氏名　溝川貴司

本論文では、遷移金属の 3d 電子間に働くクーロン相互作用と、遷移金属 3d 軌道とそれに配位してる陰イオンの p 軌道間の混成がともに強く、その両者の競合が多様な物性の源となっていると予想される、ペロブスカイト型 3d 遷移金属酸化物と II-VI 半導体中の3d 遷移金属不純物の電子状態を研究対象とした。光電子分光法、X線吸収分光法を用いた実験と、その実験結果を単一の遷移金属イオンのみ含むクラスターモデルおよびアンダーソン不純物モデルを用いて解析することにより、これらの物質の電子状態を明らかにする。遷移金属の 3d 電子間に働くクーロン相互作用 U と、陰イオンの p 軌道から遷移金属 3d 軌道への電荷移動に要するエネルギー Δ が重要なパラメーターとなっており、$\Delta < U$ ではバンドギャップの大きさが Δ で決定される電荷移動型の絶縁体、$\Delta > U$ ではバンドギャップの大きさが U で決定される Mott-Hubbard 型の絶縁体となる。さらに、遷移金属化合物の磁気的電気的な物性と電子状態との関連を調べるために、遷移金属化合物の結晶の並進対称性を正確に扱ったアンダーソン格子モデルによる計算を行った。

第 3 章では、Ni の形式価数が 3 価（$d^7$）であるペロブスカイト型 3d 遷移金属酸化物 $PrNiO_3$ の電子状態を光電子分光法、X線吸収分光法を用いて調べた。$PrNiO_3$ は、温度の増加とともに、反強磁性絶縁体から常磁性金属へと転移する。また、Pr をイオン半径

のより小さなイオンに置換して $GdFeO_3$ 型の歪みを大きくすると、金属から絶縁体への転移温度が高くなる、つまり、バンドギャップが大きくなることが報告されている。また、2重縮重の $e_g$ 軌道のうちの一方が3d電子によって占められるという軌道の自由度を持つため、その複雑な磁気構造から軌道の整列の可能性が指摘されている。まず、価電子帯およびNi 2p内殻の光電子スペクトルに見られるサテライト構造を $NiO_6$ クラスターモデルにおける配置間相互作用（CI）計算により解析した。CI法では $d^n$ 電子配置から出発して、$d^{n+1}\underline{L}$, $d^{n+2}\underline{L}^2$（$\underline{L}$ は酸素2p軌道のホールを表わす）といった電子配置との混成を正確に扱う。この解析より、$PrNiO_3$ の電荷移動エネルギーΔ、3d電子間のクーロン相互作用U、遷移金属3d軌道と酸素2p軌道との移動積分(pdσ)がそれぞれ、1.0、7.0、-1.5 eV程度と見積もられた。電荷移動エネルギーΔが小さいために、基底状態では $d^7$ と $d^8\underline{L}$ の電子配置が強く混成している、つまり、遷移金属3d軌道と酸素2p軌道が強く混成しており、また、バンドギャップの性質は典型的な電荷移動型ではなく、バンドギャップ直上の伝導帯、直下の価電子帯ともに遷移金属3d軌道と酸素2p軌道が強く混成した状態からなることが明らかになった。クラスターモデルの描像から出発してこのようなバンドギャップを考えた場合、$NiO_6$ クラスター間の相互作用の強さがバンドギャップの大きさに影響を与えることが期待される。遷移金属3d軌道と酸素2p軌道を含む格子モデルにおいてHartree-Fock (HF)近似計算を行うと、$GdFeO_3$ 型の歪みが大きくなりNi-O-Niの結合角が180度から小さくなっていくにつれて、バンドギャップが大きくなることが明らかになった。これは、$NiO_6$ クラスター間の相互作用の強さが $GdFeO_3$ 型の歪みによりとともに小さくなり、その結果、バンドギャップが大きくなることを示している。

第4章では、Cuの形式価数が3価（$d^8$）であるペロブスカイト型3d遷移金属酸化物 $LaCuO_3$ の電子状態を光電子分光法、X線吸収分光法を用いて調べた。$LaCuO_3$ は、180度のCu-O-Cuの結合角を持ち、常磁性金属である。価電子帯およびCu 2p内殻の光電子スペクトルに観測されるサテライト構造を $CuO_6$ クラスターモデルで解析することにより、電荷移動エネルギーΔ、3d電子間のクーロン相互作用U、遷移金属3d軌道と酸素2p軌道間の移動積分(pdσ)がそれぞれ、-1.0、7.0、-1.7 eV程度と見積もられた。電荷移動エネルギーΔが負の値をとるために、基底状態は $d^9\underline{L}$ の電子配置が支配的である。Cu-O-Cuの結合角が180度の $LaCuO_3$ では、$CuO_6$ クラスター間の相互作用が強いために金属となっているとみることができる。このクラスター間の強い相互作用はCu 2p X線吸収スペクトルが $CuO_6$ クラスターモデルでは説明できないことからも示唆された。$LaCuO_3$ の価電子帯の光電子スペクトルをHF近似に基づくバンド計算を出発点として調べると、サテライト構造がバンド計算では再現できないこと、Fermi準位近傍の光電子スペクトル強度がバンド計算で予測されるものよりも弱くなっていること、の2点が明らかになった。HF近似によるバンド計算の結果に3d電子間クーロン相互作用についての2次の摂動を加えると、サテライト構造はある程度再現できたが、Fermi準位近傍の光電子スペクトル強度の減少は説明できなかった。

第5章では、ペロブスカイト型の格子モデルにおいて、スピンおよび軌道の分極を許した非制限HF近似計算により、TiからCuまでのペロブスカイト型3d遷移金属酸化物の電子状態を調べた。縮重している軌道が部分的に占められている場合、一般には異なる軌道が交互に占められてスピンが強磁性的に揃った状態が、原子内の交換相互作用によって好まれる傾向がある。$RTiO_3$（$d^1$）と $RVO_3$（$d^2$）（$R$ は稀土類元素あるいはY）では、$t_{2g}$ 軌道のうちの異なる軌道が交互に占有されて整列することにより、それぞれ、F型とC型にスピンが整列した解が安定となる。これらの状態は、さらに、Jahn-Teller (JT)歪みによって安定化される。$d^4$ 高スピン（$t_{2g\uparrow}^3 e_{g\uparrow}$）$LaMnO_3$ では、$e_g$ 軌道のうちの一方が占められてF型の配置をとる解が最低であるが、JT歪みによってA型にスピンが整列した解が安定化される。$d^6$ 低スピン（$t_{2g\uparrow}^3 t_{2g\downarrow}^3$）の $LaCoO_3$ では、準安定な状態として中間スピン（$t_{2g\uparrow}^3 t_{2g\downarrow}^2 e_{g\uparrow}$）をとるものがあり、$d^4$ 高スピンと同様の理由でF型を好む。これらのHF計算の結果は基底状態での、スピンと軌道の整列はよく説明できる。しかし、特にMott-Hubbard型のギャップを持つ絶縁体では、バンドギャップの大きさが、実験結果に比べて1-2 eV程度大きく見積もられてしまい、HF近似の限界を示している。

第6章では、$LaCuO_3$ の価電子帯の光電子スペクトルを議論する際に用いた方法、つまり、HF解のまわりでの3d電子間クーロン相互作用についての2次の摂動計算を、他の様々な基底状態を持つ3d遷移金属酸化物に適用した。自己エネルギーの計算には、その運動量依存性を無視するlocal近似を用いた。電荷移動型のギャップを持つ反強磁性絶縁体のNiOでは、$LaCuO_3$ と同様にサテライト構造を得ることができるが、光電子スペクトルを完全に再現するには至らなかった。Mott-Hubbard型のギャップを持つ強磁性絶縁体 $YTiO_3$、非磁性の絶縁体 $LaCoO_3$ では、バンドギャップの大きさが実験結果とよく一致し、Mott-Hubbard型絶縁体ではHF近似を超えた電子相関の効果がバンドギャップの大きさを決めるのに重要であることが明らかになった。常磁性金属の $SrVO_3$ については、光電子スペクトルでみられているサテライト構造を説明することができた。

第7章ではII-VI半導体中の3d遷移金属不純物の電子状態を、クラスターモデルおよびアンダーソン不純物モデルにおけるCI計算によって調べた。d-d遷移による光吸収スペクトルに見られる多重項の構造や $Cd_{1-x}Mn_xTe$ の光電子、逆光電子スペクトルをパラメーターΔ, U, (pdσ)を用いて、統一的に説明することができた。得られたパラメーターを用いて、遷移金属3d軌道とそれに配位しているイオンのp軌道間の混成に由来するd-p交換相互作用の大きさを計算し、実験結果を説明することに成功した。また、II-VI半導体の陽イオンのサイトを遷移金属で完全に置換した極限とみなすことのできる遷移金属カルコゲナイドの電子状態と磁気構造の関係を格子モデルにおける非制限HF計算によって調べた。

以上の研究から、クーロン相互作用と軌道混成が競合する遷移金属化合物や遷移金属不純物の電子状態を記述するのに、CIを取り入れたクラスターモデル計算が有効であることが示された。結晶の並進対称性を有する遷移金属化合物については、光電子スペクトルのクラスターモデルによる解析から得られたパラメーターを用いて、格子モデルでHF近似計算を行うことによりその基底状態の性質をよく説明できるが、HF近似の限界のために価電子帯の光電子スペクトルの形状を再現できない。このHF解に摂動計算による自己エネルギー補正を加えると、光電子スペクトルまで含めてその電子状態を記述できることが明らかになった。

Thesis

# Electronic structure of 3*d* transition-metal compounds with competing *d*-*d* Coulomb interaction and *d*-ligand hybridization

Takashi Mizokawa

Department of Physics, Graduate School of Science, University of Tokyo

## List of abbreviations

| | |
|---|---|
| AFM | antiferromagnetic |
| CI | configuration interaction |
| FM | ferromagnetic |
| FWHM | full width at half maximum |
| HF | Hartree-Fock |
| LCAO | linear combination of atomic orbitals |
| LDA | local-density approximation |
| LNT | liquid nitrogen temperature |
| LSDA | local-spin-density approximation |
| PM | paramagnetic |
| RT | room temperature |
| SIC | self-interaction correction |
| XAS | x-ray absorption spectroscopy |
| XPS | x-ray photoemission (photoelectron) spectroscopy |
| UHV | ultra-high vacuum |
| UPS | ultra-violet photoemission (photoelectron) spectroscopy |
| ZSA | Zaanen-Sawatzky-Allen |

## Contents


Chapter 1
Introduction, motivation and scope 1

Chapter 2
Approaches to the studies of the electronic structure of 3*d* transition-metal compounds 5

2.1 High-energy spectroscopy 6
2.2 Models for 3*d* transition-metal compounds 11
2.3 Configuration-interaction cluster-model approach 13
2.4 Hartree-Fock band-structure calculation and self-energy correction 18

Chapter 3
Electronic structure of $PrNiO_3$ studied by photoemission and x-ray absorption spectroscopy 21

3.1 Introduction 22
3.2 Experimental 24
3.3 Methods of model calculations 24
3.4 Results and discussion 27
3.5 Conclusion 40

Chapter 4
Electronic structure of $LaCuO_3$ studied by photoemission and x-ray absorption spectroscopy 43

4.1 Introduction 44
4.2 Experimental 45
4.3 Results and discussion 46
4.4 Conclusion 54

Chapter 5
Unrestricted Hartree-Fock study of the ground states and single-particle excitation spectra of perovskite-type 3*d* transition-metal oxides 57

5.1 Introduction 58
5.2 Unrestricted Hartree-Fock approximation 59

5.3 Results and discussion 64
5.4 Conclusion 84

Chapter 6
Self-energy correction to the unrestricted Hartree-Fock solution of lattice models for 3*d* transition-metal oxides 87

6.1 Introduction 88
6.2 Self-energy calculation using local approach 89
6.3 Effect of low dimensionality 95
6.4 Effect of inter-site Coulomb interaction 97
6.5 Conclusion 101

Chapter 7
Electronic structure of 3*d* transition-metal impurities in semiconductors 103

7.1 Introduction 104
7.2 Configuration-interaction approach 105
7.3 Configuration-interaction calculation on cluster and Anderson impurity models 106
7.4 Unrestricted Hartree-Fock calculation on a lattice model for zinc-blende structure 123
7.5 Conclusion 125

Chapter 8
Concluding remarks 127

Acknowledgment 131

Appendix I : Matrix elements of 3*d*-3*d* Coulomb interaction

Appendix II : Matrix element of the lowest terms $E(d^n)$, the charge-transfer energy $\Delta_{eff}$ and the *d*-*d* Coulomb interaction $U_{eff}$

Appendix III : Ligand field due to non-orthogonality for the octahedral and tetrahedral clusters

References



# Chapter one

# Introduction, motivation and scope

3*d* transition-metal atoms, which are characterized by the partially filled 3*d* subshell, present us with a variety of compounds and complexes which show various physical properties including electrical, magnetic and optical as well as chemical ones. Some of the transition-metal complexes also play essential roles in biological species. In the 3*d* transition-metal compounds and complexes, many properties are originated from the localized character of the 3*d* electron, because of which, for example, the strong *d*-*d* Coulomb interaction give rise to beautiful multiplet structures observed in optical measurements. However the 3*d* orbitals, more or less, hybridize with the ligand orbitals and are extended into the ligand sites. The hybridization controls the localized versus extended character of the 3*d* electrons and affects the physical and chemical properties. The present thesis has been motivated by the question how we can describe the electronic structures of the 3*d* transition-metal compounds in which both the *d*-*d* Coulomb interaction and *d*-ligand hybridization are strong. In this thesis, electronic structures of perovskite-type 3*d* transition-metal oxides and 3*d* transition-metal impurities in II-VI semiconductors, in which the strong *d*-*d* Coulomb interaction and *d*-ligand hybridization are competing, are investigated both experimentally and theoretically.

In the field of solid state physics, many researchers have been fascinated by the interesting physical properties of the 3*d* transition-metal compounds and have been trying to clarify the origin of the properties by investigating their electronic structures. Especially, the metallic versus insulating behavior of the 3*d* transition-metal compounds has been extensively studied in these decades. Mott and Hubbard have shown that the strong *d*-*d* Coulomb interaction is essential to explain why some of the 3*d* transition-metal compounds with partially filled 3*d* band exist as insulators and the others as metals [Mott, 1949; Hubbard, 1963, 1964a, 1964b]. When the *d*-*d* Coulomb interaction is larger than the dispersional part of the 3*d* bands, 3*d* electrons are itinerant and the compound becomes metallic. On the other hand, when the *d*-*d* Coulomb interaction is larger than the band width, 3*d* electrons are localized and the magnitude of the band gap is determined by the *d*-*d* Coulomb interaction.

Fujimori and Minami [1984] have shown that the band gap of NiO is not determined by *d*-*d* Coulomb interaction $U$ but by ligand-to-*d* charge-transfer energy $\Delta$ by analyzing the photoemission spectrum with the configuration-interaction (CI) cluster-model approach. Based on the local-cluster and single-impurity approach, Zaanen, Sawatzky and Allen (ZSA) [1985] and Hüfner [1985] have proposed a classification scheme, where the transition-metal compounds can be classified into two regimes according to the relative magnitude of $\Delta$ and $U$. In the Mott-Hubbard regime, $\Delta > U$, the band gap is determined by charge fluctuations of a *d*-*d* type, $d^n + d^n \rightarrow d^{n+1} + d^{n-1}$ and its magnitude is essentially given by $\sim U$. In the charge-transfer regime, where $\Delta < U$, charge fluctuations of a type $d^n + d^n \rightarrow d^{n+1} + d^n\underline{L}$ constitute a *p*-*d* type band gap, whose magnitude is $\sim \Delta$. The CI cluster-model approach and the ZSA scheme have played an important role to interpret high-energy spectroscopic data including photoemission spectra of the 3*d* transition-metal compounds. The ZSA scheme tells us that the relative strength of the *d*-ligand hybridization to $\Delta$ or $U$ determines the metallic versus insulating behavior. However, in order to fully describe the metal-insulator transition, the local-cluster and single-impurity models are insufficient and studies on lattice models are required. In Chapter 2, after high-energy spectroscopy, which is a powerful tool to study the electronic structure of the 3*d* transition-metal compounds, is introduced, the configuration-interaction local-cluster approach for 3*d* transition-metal compounds is briefly reviewed. As a method complementary to the local-cluster approach, the unrestricted Hartree-Fock (HF) calculation and perturbation expansion on lattice models are also introduced.



The discovery of the high $T_c$ copper oxide in 1986 [Bednorz and Müller, 1986], whose parent material is layered-perovskite-type $Cu^{2+}$ oxides with a charge-transfer-type band gap, has accelerated the research of the 3*d* transition-metal oxides. Especially the metal-insulator transition of the perovskite-type 3*d* transition-metal oxides have attracted much interest. The 3*d* transition-metal oxides, especially with high valence such as $Cu^{3+}$ and $Ni^{3+}$, are expected to be stages in which both strong *d*-*d* Coulomb interaction and *d*-ligand hybridization play important roles. In Chapter 3, the photoemission and x-ray absorption study of $PrNiO_3$, which shows metal-insulator transition, is presented. Both local-cluster approach and HF band-structure calculations are applied in order to clarify the origin of the metal-insulator transition. In Chapter 4, a formally $Cu^{3+}$, metallic oxide, $LaCuO_3$, is studied by photoemission and x-ray absorption spectroscopy and subsequent local-cluster and HF band-structure calculations. Key questions are how far the local-cluster picture can survive in the perovskite-type 3*d* transition-metal oxides and to what extent the HF band-structure calculations can describe their electronic structures.

In Chapter 5, the spin- and orbital- unrestricted HF calculations are performed for the perovskite-type *d*-*p* lattice models. Spin and orbital orderings in the perovskite-type 3*d* transition-metal oxides are extensively studied. In Chapter 6, the self-energy correction to the HF solution is investigated using the local approximation, which neglects the momentum dependence of the self-energy. It is shown that electron correlation beyond the HF approximation is essential to explain the photoemission spectra of the various 3*d* transition-metal oxides. The effects of the momentum dependence of the self-energy is investigated in low-dimensional systems such as the $CuO_3$ chain by the expansion around the local approximation. As another origin of the momentum dependence of the self-energy, the effect of the inter-site Coulomb interaction is also discussed.

3*d* transition-metal impurities in semiconductors have been a subject of extensive investigations from their technological importance as well as from the viewpoint of basic physics [Zunger, 1986]. Especially for the cation substituted transition-metal impurities in II-VI semiconductors, the transition-metal ions are coordinated by chalchogen ions and the CI local-cluster approach can be applied to investigate their electronic structures. In Chapter 7, the electronic structures of the 3*d* transition-metal impurities in semiconductors have been studied

mainly using the local-cluster calculations. The electronic structures of the 3*d* transition-metal chalcogenides, which can be viewed as the 100% substituted limit, are also investigated by means of the HF band-structure calculation. These calculations give us a clue to link between the local-cluster picture, which is applicable to the 3*d* transition-metal impurities in semiconductors, and band picture.

Finally, conclusions of the present work and future prospects are summarized in Chapter 8.



# Chapter two

# Approaches to the studies of the electronic structure of 3*d* transition-metal compounds

In this chapter, a brief introduction to the high-energy spectroscopy of solids is given for readers who are not familiar with this field. Models are also introduced to interpret the high-energy spectroscopy of the 3*d* transition-metal compounds and to extract pieces of information on their electronic structures. The configuration-interaction cluster-model approach and the unrestricted Hartree-Fock and self-energy correction method on lattice models are explained in detail.

## 2.1. High-energy spectroscopy

### 2.1.1. Photoemission spectroscopy

A schematic drawing of photoemission experiment and the principle of the photoemission process in a solid is illustrated in Figs. 2.1 and 2.2 [Cardona and Ley, 1978; Hüfner, 1995]. A gas discharge lamp and an x-ray tube are used as laboratory light sources for ultraviolet photoelectron spectroscopy (UPS) and for x-ray photoelectron spectroscopy (XPS), respectively. Synchrotron radiation from a storage ring can also be used as a photon source. An electron bounded in the solid is excited and liberated by the incident photon and escapes into the vacuum. The kinetic energy of the emitted electron or photoelectron is analyzed using an energy analyzer. The kinetic energy is given by the retarding energy plus the pass energy of the analyzer, which is determined by the geometrical arrangement of the electrodes of the analyzer, the voltage difference between them and their work function. By knowing the photon energy $h\nu$ and the kinetic energy of the photoelectron $E_k$ measured from the sample Fermi level we can determine the binding energy $E_B$ through the relation

$$E_k = h\nu - E_B \,. \qquad (2.1)$$

If the number of the photoelectrons is plotted as a function of the binding energy, the obtained energy distribution curve can be viewed as a replica of the electron energy distribution in the solid (see Fig. 2.2). The electron escape depth, which is mainly determined by plasmon energy losses in the solid, is ranging from 2 to 20 Å in the electron kinetic energy range of photoemission spectroscopy [Shirley, 1978; Hüfner, 1995]. Therefore, special care has to be taken to avoid surface contamination or degradation. Measurements have to be done under an ultra-high vacuum (UHV) and we have to make efforts to obtain a fresh surface. Although it is very difficult to estimate to what extent a spectrum is representative of bulk, we can judge that the spectrum is not affected by surface contamination or degradation by monitoring lack of structures which are empirically found to be due to surface contributions.

Let us consider a photoemission process from a many-electron system following the formulation by Kotani [1987] and Gunnarsson and Schönhammer [1987]. Here, for simplicity, the scattering of the photoelectron during its transportation to the surface and the effect of its penetration from the solid to the vacuum are ignored. The system of electrons can be divided into three sub-systems, outer electrons, core electrons and a photoelectron. The Hamiltonian is given by

$$H = H_{\rm v} + H_{\rm vc} + \sum_c (-\varepsilon_c) a_c a_c^+ + H_{\rm vk} + \sum_k \varepsilon_k a_k^+ a_k \,, \qquad (2.2)$$



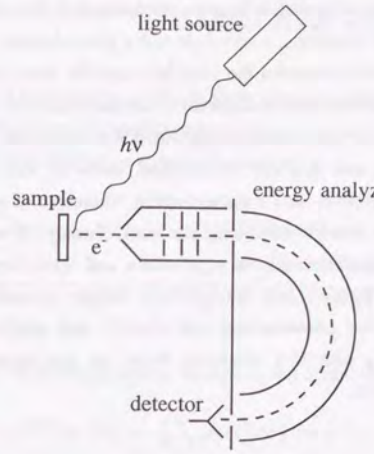


**Fig. 2.1.** Schematic drawing of a photoemission experiment.

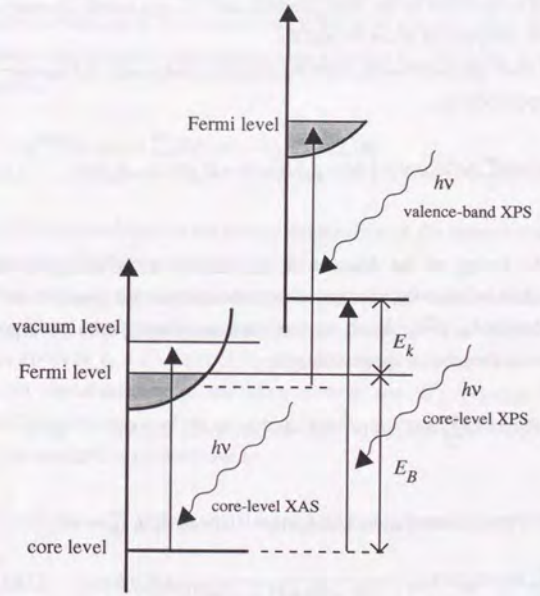


**Fig. 2.2.** Relation between the energy distribution of electrons in a solid and that of photoelectrons.

where $a_c$ and $a_k^+$ are creation operators of a core hole and a photoelectron. The first, third and fifth terms represent systems of outer electrons, a core hole and a photoelectron, respectively. The second term describes an interaction between the core hole and the outer electrons. The fourth term expresses an interaction between the photoelectron and the remaining electrons (the outer electrons and core hole). The eigenvalue and eigenfunction of the initial state with $N$ outer electrons can be denoted by $E_0(N)$ and $|E_0(N)\rangle$. In the final states of the valence band photoemission, we have $N$-1 outer electrons and a photoelectron. Therefore, if we neglect the interaction between the photoelectron and the remaining electrons, namely, if we neglect the fourth term of (2-2) (the sudden approximation), the eigenvalues and wave functions of the final states are expressed as $\varepsilon_k + E_f(N\text{-}1)$ and $|k\rangle|E_f(N\text{-}1)\rangle$, where $\varepsilon_k$ and $|k\rangle$ are the eigenvalues and eigenfunctions of the photoelectron and $E_f(N\text{-}1)$ and $|E_f(N\text{-}1)\rangle$ are the eigenvalues and eigenfuctions of $H_v$ with $N$-1 electrons. Here, we introduce an operator representing the photoexcitation process,

$$M_i^+ = \sum_k T_{ki}\, a_k^+ a_i \ , \qquad (2.3)$$

where $a_i^+$ is a creation operators of an outer electron and $T_{ki}$ is a matrix element of the dipole operator between the one-particle states $|i\rangle$ and $|k\rangle$.

In the valence band photoemission, from the Fermi's golden rule, the number of electrons with energy $\varepsilon$ is proportional to

$$I(\varepsilon) = \sum_{k,j} \left| \langle E_j(N-1)|\langle k| \sum_i M_i^+ |E_0(N)\rangle \right|^2 \delta(\varepsilon-\varepsilon_k)\, \delta(\varepsilon - h\nu + E_j(N-1) - E_0(N)) \ , \qquad (2.4)$$

where $\varepsilon$ is the kinetic energy of the detected electron and $h\nu$ is the energy of the incidental photon. $|E_0(N)\rangle$ in (2.4) includes the vacuum of the photoelectron subspace. If we assume that the energy dependence of $\Sigma_k T_{ki}{}^* T_{ki'}\, \delta(\varepsilon\text{-}\varepsilon_k)$ is negligible and that $T_{ki}$ does not depend on $i$, $I(\varepsilon)$ is proportional to the single-particle spectral function,

$$\rho^{\mathrm{PES}}(\varepsilon - h\nu) = \sum_j \left| \langle E_j(N-1)| \sum_i a_i |E_0(N)\rangle \right|^2 \delta(\varepsilon - h\nu + E_j(N-1) - E_0(N)) \ . \qquad (2.5)$$

(2.5) is transformed through the relation $1/(x + i\eta) = \mathrm{P}1/x - i\pi\, \delta(x)$, $\eta \to +0$,

$$\rho^{\mathrm{PES}}(\varepsilon - h\nu) = -\frac{1}{\pi} \sum_{i,i'} \mathrm{Im} \langle E_0(N)| a_{i'}^+ \frac{1}{\varepsilon - h\nu + i\eta + H_v - E_0(N)}\, a_i |E_0(N)\rangle \ . \qquad (2.6)$$

In the case of the inverse photoemission process, the spectral function is also given by



$$\rho^{\mathrm{IPES}}(\varepsilon - h\nu) = -\frac{1}{\pi} \sum_{i,i'} \mathrm{Im} \langle E_0(N)| a_{i'} \frac{1}{\varepsilon - h\nu + i\eta - H_v + E_0(N)}\, a_i^+ |E_0(N)\rangle \ , \qquad (2.7)$$

where $\varepsilon$ is the kinetic energy of the incident electron and $h\nu$ is the energy of the detected photon. The spectral functions of the photoemission and inverse photoemission processes are related to the retarded Green's function at zero temperature,

$$G_{ii'}^{\mathrm{R}}(z) = -i \int_{-\infty}^{\infty} \theta(t)\, \langle E_0(N)|\, [a_i(t), a_{i'}^+]_+ \,|E_0(N)\rangle\, e^{izt}\, dt$$

$$= \langle E_0(N)| a_{i'}^+ \frac{1}{z + H_v - E_0(N)}\, a_i |E_0(N)\rangle + \langle E_0(N)| a_i \frac{1}{z - H_v + E_0(N)}\, a_{i'}^+ |E_0(N)\rangle \ , \qquad (2.8)$$

where $[\ ,\ ]_+$ is an anticommutator. Therefore, we obtain the relation

$$\rho^{\mathrm{PES}}(\varepsilon - h\nu) + \rho^{\mathrm{IPES}}(\varepsilon - h\nu) = -\frac{1}{\pi} \sum_{i,i'} \mathrm{Im} G_{ii'}^{\mathrm{R}}(\varepsilon - h\nu + i\eta) \ , \eta \to +0 \ . \qquad (2.9)$$

When a Hartree-Fock-type mean-filed approximation is applied to the interacting outer electrons, the wave function of the ground state is given by a single Slater determinant which is constructed from single-particle eigenstates with energies $\varepsilon_i$. By using Koopmans' theorem, (2.9) is reduced to

$$\rho^{\mathrm{PES}}(\varepsilon - h\nu) + \rho^{\mathrm{IPES}}(\varepsilon - h\nu) = \sum_i \delta(\varepsilon - h\nu - \varepsilon_i) \ . \qquad (2.10)$$

The r. h. s. of (2.10) is nothing but the energy distribution of the ground-state density of states obtained by the mean-field approximation.

In the final states of core-level photoemission, we have $N$ outer electrons, a core hole and a photoelectron. If we use the sudden approximation, the eigenvalues and wave functions of the final states are given by $\varepsilon_k + E^c{}_j(N)$ and $|k\rangle|E^c{}_j(N)\rangle$, respectively, where $-\varepsilon_k$ and $|k\rangle$ are the eigenvalues and eigenfunctions of the photoelectron and $E^c{}_j(N)$ and $|E^c{}_j(N)\rangle$ are the eigenvalues and eigenfunctions of the system of $N$ outer electrons and a core hole. The number of electrons with energy $\varepsilon$ is proportional to

$$I^{\mathrm{cPES}}(\varepsilon) = \sum_{k,j} \left| \langle E_j^c(N)|\langle k| \sum_c M_c^+ |E_0(N)\rangle \right|^2 \delta(\varepsilon-\varepsilon_k)\, \delta(\varepsilon - h\nu + E_j^c(N) - E_0(N)) \ . \qquad (2.11)$$

If we assume that the energy dependence of $\Sigma_k T_{kc}{}^* T_{kc'}\, \delta(\varepsilon\text{-}\varepsilon_k)$ is negligible and that $T_{kc}$ does not depend on $c$, $I^{\mathrm{cPES}}(\varepsilon)$ is proportional to the spectral function of core-level photoemission process,

$$\rho^{cPES}(\varepsilon-h\nu)=\sum_j\left|<E^c_j(N)|\sum_c a_c|E_0(N)>\right|^2\delta(\varepsilon-h\nu+E^c_j(N)-E_0(N))\ , \quad (2.12)$$

If the multiplet coupling between the outer electrons and core hole is neglected, $E^c_j(N)$ and $|E^c_j(N)>$ are expressed by $-\varepsilon_c+E'_j(N)$ and $|c>|E'_j(N)>$, respectively, where $-\varepsilon_c$ and $|c>$ are the eigenvalues and eigenfunctions of the core hole and $E'_j(N)$ and $|E'_j(N)>$ are the eigenvalues and eigenfunctions of the system of $N$ outer electrons interacting with a core hole. As a result, the intensity is proportional to

$$\rho^{cPES}(\varepsilon-h\nu)=\sum_c\rho^{cPES}_c(\varepsilon-h\nu)=\sum_c\sum_j\left|<E'_j(N)|E_0(N)>\right|^2\delta(\varepsilon-h\nu-\varepsilon_c+E'_n(N)-E_0(N))\ , \quad (2.13)$$

### 2.1.2. X-ray absorption spectroscopy

X-ray absorption spectroscopy (XAS) is made with use of synchrotron radiation and monochromator. A core electron is excited to an unoccupied state in the solid by the incident photon. The absorption of the photon can be measured in the transmission mode, in the fluorescence-yield mode or in the electron-yield mode [Fuggle, 1992]. The measurement in the electron yield mode is easily applicable to any types of samples, but we have to pay attention to surfaces of samples because it is as sensitive to surface contamination as photoemission. If the absorption of the photon is plotted as a function of the photon energy, the curve reflects the unoccupied density of states.

In the XAS process, the absorption of the photon with the energy $\varepsilon$ is proportional to

$$I^{cXAS}(\varepsilon)=\sum_j\left|<E^c_j(N+1)|\sum_c M^+_c|E_0(N)>\right|^2\delta(\varepsilon-E^c_j(N+1)-E_0(N))\ . \quad (2.14)$$

If we neglect the multiplet coupling between the outer electrons and core hole, (2.14) can be transformed into

$$I^{cXAS}(\varepsilon)=\sum_c I^{cXAS}_c(\varepsilon)$$
$$=\sum_c\sum_j\left|<E'_j(N+1)|\sum_i T_{ic}a^+_i|E_0(N)>\right|^2\delta(\varepsilon-\varepsilon_c+E'_j(N+1)-E_0(N))\ , \quad (2.15)$$

If we assume that $T_{ic}$ does not depend on $i$ and $c$, $I^{cXAS}(\varepsilon)$ is proportional to the spectral function of x-ray absorption process,



$$\rho^{cXAS}_c(\varepsilon)=\sum_i\sum_j\left|<E'_j(N+1)|a^+_i|E_0(N)>\right|^2\delta(\varepsilon-\varepsilon_c+E'_j(N+1)-E_0(N))\ , \quad (2.16)$$

If the interaction between the core hole and the outer electrons is neglected, the spectral function directly reflects that of the electron addition process.

### 2.2. Models for 3*d* transition-metal compounds

The Anderson lattice model (*d-p* model) has been considered to be a good model to describe a system where localized transition-metal 3*d* orbitals hybridize with extended ligand *p* orbitals. The Hamiltonian of the Anderson lattice model is given by (2.17) - (2.20):

$$H_v=H_d+H_p+H_{pd}\ , \quad (2.17)$$

$$H_d=\varepsilon^0_d\sum_{i,m\sigma}d^+_{i,m\sigma}d_{i,m\sigma}+\sum_{i,m\sigma,m'\sigma'}h_{m\sigma,m'\sigma'}d^+_{i,m\sigma}d_{i,m'\sigma'}$$
$$+\sum_i\sum_{m\sigma,m'\sigma',m''\sigma'',m'''\sigma'''}U_{m\sigma,m'\sigma',m''\sigma'',m'''\sigma'''}d^+_{i,m\sigma}d_{i,m'\sigma'}d^+_{i,m''\sigma''}d_{i,m'''\sigma'''}\ , \quad (2.18)$$

$$H_p=\varepsilon_p\sum_{\vec{k},l,\sigma}p^+_{\vec{k},l\sigma}p_{\vec{k},l\sigma}+\sum_{\vec{k},l>l',\sigma}V^{pp}_{\vec{k},ll'}p^+_{\vec{k},l\sigma}p_{\vec{k},l'\sigma}+\text{H. c.}\ , \quad (2.19)$$

$$H_{pd}=\sum_{\vec{k},l,i,m,\sigma}V^{pd}_{\vec{k},l,i,m}p^+_{\vec{k},l\sigma}d_{i,m\sigma}+\text{H. c.}\ , \quad (2.20)$$

where $i$ and $\vec{k}$ label the unit cell and the wave vector in the Brillouine zone. $m$ and $l$ are orbital indices of the transition-metal 3*d* and ligand *p* orbitals, respectively. The second term of the Hamiltonian $H_d$ represents the on-site Coulomb interactions, which is expressed in terms of Racah parameters [Tanabe and Sugano, 1954a, 1954b; Kamimura *et al.*, 1969; Sugano *et al.*, 1970; Griffith 1971] or Kanamori parameters [Kanamori, 1963] (see Appendix I). The Hamiltonian $H_{pd}$ describes the hybridization between the 3*d* orbitals and the Bloch states constructed from the ligand *p* orbitals. The transfer integrals are described in terms of the Slater-Koster parameters ($pd\sigma$) and ($pd\pi$) [Slater and Koster, 1954].

If the localized 3*d* orbitals at only one site are taken into account, namely, the translational symmetry of the localized 3*d* orbitals is neglected, the Anderson lattice model is reduced to the Anderson impurity model. The Hamiltonian of the Anderson impurity model is given by replacing (2.18) and (2.20) by

$$H_d = \varepsilon_d^0 \sum_{m\sigma} d_{m\sigma}^+ d_{m\sigma} + \sum_{m\sigma, m'\sigma'} h_{m\sigma, m'\sigma'} d_{m\sigma}^+ d_{m'\sigma'} + \sum_{m\sigma, m'\sigma', m''\sigma'', m'''\sigma'''} U_{m\sigma, m'\sigma', m''\sigma'', m'''\sigma'''} d_{m\sigma}^+ d_{m'\sigma'}^+ d_{m''\sigma''} d_{m'''\sigma'''} \quad (2.21)$$

and

$$H_{pd} = \sum_{\underline{k}, l, m, \sigma} V_{\underline{k}, l, m}^{pd} p_{\underline{k}, l\sigma}^+ d_{m\sigma} + \text{H. c.} , \quad (2.22)$$

respectively. The Hamiltonian becomes tractable if we make the transformation

$$|V_m(\varepsilon)|^2 = \sum_{\underline{k}, l} |V_{\underline{k}, l, m}^{pd}|^2 \delta(\varepsilon - \varepsilon_{\underline{k}}) . \quad (2.23)$$

As a result, the Hamiltonian of the Anderson single-impurity model is given by (2.17), (2.21),

$$H_p = \int_{-W/2}^{W/2} d\varepsilon \, \varepsilon \, p_{\varepsilon\sigma}^+ p_{\varepsilon\sigma} , \quad (2.24)$$

and

$$H_{pd} = \int_{-W/2}^{W/2} d\varepsilon \, V_m(\varepsilon) p_{\varepsilon\sigma}^+ d_{m\sigma} + \text{H. c.} , \quad (2.25)$$

where $W$ is the band with of the $p$ band. Historically, many calculations using the Anderson impurity model have been performed on Ce mixed-valence compounds to explain their photoemission and inverse-photoemission spectra and to describe their electronic structures [Gunnarsson and Schönhammer, 1987]. Zaanen [1986] has applied the impurity model to 3*d* transition-metal compounds and have shown that the model works well.

It is still hard to solve the Anderson single-impurity model numerically including both the intra-atomic multiplet effect of localized 3*d* orbitals and the finite band width of the host band states. When it is more important to take into account the multiplet effect than the finite band width, we can limit the calculation to a cluster including only one transition-metal site and nearest neighbor ligand sites. The Hamiltonian of the cluster model is given by (2.17), (2.21),

$$H_p = \sum_{m, \sigma} \varepsilon_{p, m} p_{m\sigma}^+ p_{m\sigma} , \quad (2.26)$$

and



$$H_{pd} = \sum_m V_m p_m^+ d_m + \text{H. c.} , \quad (2.27)$$

where $p_m^+$ is a creation operator of an electron in a ligand molecular orbital with symmetry $m$.

### 2.3. Configuration-interaction cluster-model approach

The configuration-interaction (CI) calculations on the cluster model have been successfully applied to reproduce the valence-band [Fujimori and Minami, 1984; Eskes *et al* ., 1990] and core-level [van der Laan *et al*., 1981; Zaanen *et al*., 1986; Park *et al*., 1988; Okada and Kotani, 1991; Bocquet *et al*., 1992b] photoemission spectra of the 3*d* transition-metal compounds. In this section, a brief description of the CI cluster-model calculation is presented. In the CI scheme, the ground state and its charge-conserving excited states, which we call $N$-electron states, are spanned by $d^n$, $d^{n+1}\underline{L}$,...,$d^{10}\underline{L}^{10-n}$ configurations, where $\underline{L}$ denotes a ligand hole. The wave function of the ground state of the $N$-electron states is written as

$$|E_0(N)> = \sum_{m=0}^{10-n} \sum_{i=1}^{S_{n+m,m}} \alpha_{m,i}^0 \, |d^{n+m}\underline{L}^m, i> , \quad (2.28)$$

where $|d^{n+m}\underline{L}^m, i>$ and $S_{n+m,m}$ represent an $i$-th component and the number of basis of the $d^{n+m}\underline{L}^m$ configuration, respectively. The Hamiltonian is given by

$$\boldsymbol{H} = \begin{pmatrix} E_n \boldsymbol{I} + \boldsymbol{X}_n^0 & \boldsymbol{V}_1 & \boldsymbol{0} & \\ \boldsymbol{V}_1 & (E_n+\Delta)\boldsymbol{I} + \boldsymbol{X}_{n+1}^1 & \boldsymbol{V}_2 & \\ \boldsymbol{0} & \boldsymbol{V}_2 & (E_n+2\Delta+U)\boldsymbol{I} + \boldsymbol{X}_{n+2}^2 & \cdots \\ & \vdots & & \end{pmatrix} . \quad (2.29)$$

$E_n \equiv E(d^n)$, $\Delta \equiv E(d^{n+1}\underline{L}) - E(d^n)$ is the charge-transfer energy, $U \equiv E(d^{n-1}) + E(d^{n+1}) - 2E(d^n)$ is the repulsive $d$-$d$ Coulomb interaction energy, where $E(d^{n+m}\underline{L}^m)$ is the center of gravity of the $d^{n+m}\underline{L}^m$ configuration. $\boldsymbol{I}$ is a unit matrix and $\boldsymbol{X}_{n+m}^m$ represents the Coulomb matrix for $d^{n+m}\underline{L}^m$ configuration relative to its center of gravity, whose trace is zero by definition. $\boldsymbol{V}_n$, represents hybridization between the $d^{n+n'-1}\underline{L}^{n'-1}$ configuration and the $d^{n+n'}\underline{L}^{n'}$ configuration, which is expressed using the transfer integrals. The energy of the ground state $E_0(N)$ is obtained by diagonalizing the matrix of (2.29). The final states of the photoemission process, namely, the eigenstates of the ($N$-1)-electron system, are expressed as

$$|E_j(N-1)> = \sum_{m=0}^{11-n} \sum_{i=1}^{S_{n+m-1,m}} \beta_{m,i}^{j} |d^{n+m-1}\underline{L}^m, i> . \quad (2.30)$$

The Hamiltonian is given by

$$\boldsymbol{H} = \begin{pmatrix} E_{n-1}\boldsymbol{I}+X_{n-1}^{0} & V'_1 & 0 & \\ V'_1 & (E_{n-1}+\Delta-U)\boldsymbol{I}+X_n^1 & V'_2 & \\ 0 & V'_2 & (E_{n-1}+2\Delta-U)\boldsymbol{I}+X_{n+1}^2 & \cdots \\ & \vdots & & \end{pmatrix} , \quad (2.31)$$

where $V'_{n'}$ is the transfer integral between the $d^{n+n'-2}\underline{L}^{n'-2}$ and $d^{n+n'-1}\underline{L}^{n'-1}$ configurations. The energies and wave functions of the final states are obtained by diagonalizing the Hamiltonian (2.31). The lowest energy level of the final state is the first ionization level, the energy of which is denoted by $E_0(N\text{-}1)$. Using the sudden approximation, the 3*d* photoemission intensity of the *j*-th final state is given by

$$I_j^{\mathrm{PES}} \propto \left| \sum_{m=0}^{10-n} \sum_{i=1}^{S_{n+m,m}} \sum_{i'=1}^{S_{n+m-1,m}} \alpha_{m,i}^{0} \beta_{m,i'}^{j} T_{m,ii'} \right|^2 , \quad (2.32)$$

where $T_{m,ii'}$ are transition matrix elements between the $d^{n+m}\underline{L}^m$ and $d^{n+m-1}\underline{L}^m$ configurations. The final states of the inverse photoemission process or the eigenstates of $(N+1)$-electron system are expressed as

$$|E_j(N+1)> = \sum_{m=0}^{9-n} \sum_{i=1}^{S_{n+m+1,m}} \gamma_{m,i}^{j} |d^{n+m+1}\underline{L}^m, i> , \quad (2.33)$$

The Hamiltonian of the $(N+1)$-electron system can be constructed in the same way.

$$\boldsymbol{H} = \begin{pmatrix} E_{n+1}\boldsymbol{I}+X_{n+1}^{0} & V''_1 & 0 & \\ V''_1 & (E_{n+1}+\Delta+U)\boldsymbol{I}+X_{n+2}^1 & V''_2 & \\ 0 & V''_2 & (E_{n+1}+2\Delta+3U)\boldsymbol{I}+X_{n+3}^2 & \cdots \\ & \vdots & & \end{pmatrix} . \quad (2.34)$$



The lowest energy level of the $(N+1)$-electron system or the affinity level is denoted by $E_0(N+1)$, which is obtained by diagnalizing (2.34). The magnitude of the conductivity gap in the cluster scheme is given by

$$E_{\mathrm{gap}} = E_0(N\text{-}1) + E_0(N+1) - 2E_0(N) . \quad (2.35)$$

Final states of the core-level photoemission process are expressed as

$$|E_j^c(N)> = \sum_{m=0}^{10-n} \sum_{i=1}^{S^c_{n+m,m}} \alpha_{m,i}^{c,j} |\underline{c}d^{n+m}\underline{L}^m, i> , \quad (2.36)$$

where $\underline{c}$ denotes a core hole. The Hamiltonian is given by

$$\boldsymbol{H} = \begin{pmatrix} E_n^c\boldsymbol{I}+X_n^{c,0} & V_1^c & 0 & \\ V_1^c & (E_n^c+\Delta-Q)\boldsymbol{I}+X_{n+1}^{c,1} & V_2^c & \\ 0 & V_2^c & (E_n^c+2\Delta-2Q+U)\boldsymbol{I}+X_{n+2}^{c,2} & \cdots \\ & \vdots & & \end{pmatrix} . \quad (2.37)$$

$E_n^c \equiv E(\underline{c}d^n)$ and $\boldsymbol{X}_{n+m}^{c,m}$ represents the Coulomb matrix of the $\underline{c}d^{n+m}\underline{L}^m$ configuration with respect to the center of gravity, whose trace is zero by definition. $\boldsymbol{V}_{n'}^c$ represents transfer integrals between $\underline{c}d^{n+n'-1}\underline{L}^{n'-1}$ and $\underline{c}d^{n+n'}\underline{L}^{n'}$. $Q$ is the multiplet-averaged attractive Coulomb interaction energy between the core hole and the 3*d* electron. The intensity of the core-level photoemission spectrum is given by

$$I_j^{\mathrm{cPES}} \propto \left| \sum_{m=0}^{10-n} \sum_{i=1}^{S_{n+m,m}} \sum_{i'=1}^{S^c_{n+m,m}} \alpha_{m,i}^{0} \alpha_{m,i'}^{c,j} T_{m,ii'}^{c} \right|^2 , \quad (2.38)$$

The final states of the core-level XAS process are expressed as

$$|E_j^c(N+1)> = \sum_{m=0}^{9-n} \sum_{i=1}^{S^c_{n+m+1,m}} \gamma_{m,i}^{c,j} |\underline{c}d^{n+m+1}\underline{L}^m, i> . \quad (2.39)$$

The Hamiltonian for the final states of the core-level XAS is given by

$$\boldsymbol{H}=\begin{pmatrix} E^{c}_{n+1}\boldsymbol{I}+\boldsymbol{X}^{c,0}_{n+1} & \boldsymbol{V}''^{c}_{1} & \boldsymbol{0} \\ \boldsymbol{V}''^{c}_{1} & (E^{c}_{n+1}+\Delta-Q+U)\boldsymbol{I}+\boldsymbol{X}^{c,1}_{n+2} & \boldsymbol{V}''^{c}_{2} \\ \boldsymbol{0} & \boldsymbol{V}''^{c}_{2} & (E^{c}_{n+1}+2\Delta-2Q+3U)\boldsymbol{I}+\boldsymbol{X}^{c,2}_{n+3}\cdots \\ & \vdots & \end{pmatrix}. \quad (2.40)$$

The intensity of the XAS spectrum is given by

$$I_j^{\mathrm{cXAS}} \propto \left| \sum_{m=0}^{10-n} \sum_{i=1}^{S_{n+m,m}} \sum_{i'=1}^{S^{c}_{n+m+1,m}} \alpha^{0}_{m,i}\gamma^{c,j}_{m,i'}T^{\mathrm{cXAS}}_{m,ii'} \right|^2 . \quad (2.41)$$

In the cluster-model calculations for the valence-band spectra, we have three adjustable parameters which are to be determined to reproduce the experimental results: $\Delta$, $U$ and $(pd\sigma)$. The ratio $(pd\sigma)/(pd\pi)$ is fixed to be ~-2.2 [Mattheiss, 1972; Harrison, 1989]. The multiplet splitting of the $d^n$ configuration due to intra-atomic Coulomb and exchange interactions are taken into account through Racah parameters, $A$, $B$ and $C$. The multiplet-averaged 3*d*-3*d* Coulomb interaction $U$ and charge-transfer energy $\Delta$ for $d^n$ are given by $A$ - 14/9$B$ + 7/9$C$ and $\varepsilon_d^0$ - $\varepsilon_p$ + $nU$, respectively, where $\varepsilon_d^0$ and $\varepsilon_p$ are the bare energy levels of the 3*d* and 2*p* orbitals. For the transition-metal 2*p* core-level XPS and XAS, $Q$ is added to the above adjustable parameters. The multiplet coupling between the transition-metal 2*p* and 3*d* electrons is expressed in terms of Slater integrals $F^2$, $G^1$ and $G^3$ [Slater, 1960; Yamaguchi *et al.*, 1982a, 1982b].

We have included the crystal-field splitting $10Dq$ which arises from the non-orthogonality between the atomic oxygen 2*p* and transition-metal 3*d* orbitals [Harrison, 1989]. The overlap integrals can be deduced from the linear-combination-of-atomic-orbitals (LCAO) fitting of the band-structure calculations by Mattheiss [1972]. We have assumed the ratio of the overlap integrals $S_\sigma$ and $S_\pi$ to the transfer integrals $(pd\sigma)$ and $(pd\pi)$ to be ~ –0.06 $\mathrm{eV}^{-1}$. The $10Dq$ from the non-orthogonality is expressed using the overlap and transfer integrals (see Appendix III).

In general, it is hard to reproduce both the valence-band and core-level photoemission spectra using the same parameter set in the cluster-model calculations because the final states have different numbers of 3*d* electrons and core hole. In this work, configuration dependence of the transfer integrals has been taken into account to make it possible to reproduce the valence-band and transition-metal 2*p* core-level XPS spectra with the same parameter set. Following Gunnarsson and Jepsen [1989], we have assumed that the transfer integrals between $d^{n-1}\underline{L}^m$ and $d^n\underline{L}^{m+1}$ are 80% of those between $d^n\underline{L}^m$ and $d^{n+1}\underline{L}^{m+1}$ and that those between $\underline{c}d^n\underline{L}^m$ and $\underline{c}d^{n+1}\underline{L}^{m+1}$ are 70% of those between $d^n\underline{L}^m$ and $d^{n+1}\underline{L}^{m+1}$.



In order to include the effect of the finite width of the ligand band, we have to exploit the Anderson impurity model for a transition-metal ion embedded in the filled $p$ band with band width $W$. For simplicity, we neglect the multiplet coupling of the $d^n$ configuration. In the CI scheme, the wave function of the ground state of the $N$-electron system is expressed as

$$|E_0(N)\rangle=\alpha_0^0|d^n\rangle+\int_{-W/2}^{W/2}d\varepsilon\,\alpha_1^0(\varepsilon)|d^{n+1}\underline{L}(\varepsilon)\rangle+\int_{-W/2}^{W/2}d\varepsilon d\varepsilon'\,\alpha_2^0(\varepsilon,\varepsilon')|d^{n+2}\underline{L}(\varepsilon)\underline{L}(\varepsilon')\rangle+\ldots, \quad (2.42)$$

where $\underline{L}(\varepsilon)$ denotes a ligand hole with energy $\varepsilon$. For example, the final states of the valence-band photoemission or the wave functions of the $(N$-1)-electron system are expressed as

$$|E_j(N-1)\rangle=\beta_0^j|d^{n-1}\rangle+\int_{-W/2}^{W/2}d\varepsilon\,\beta_1^j(\varepsilon)|d^n\underline{L}(\varepsilon)\rangle+\int_{-W/2}^{W/2}d\varepsilon d\varepsilon'\,\beta_2^j(\varepsilon,\varepsilon')|d^{n+1}\underline{L}(\varepsilon)\underline{L}(\varepsilon')\rangle+\ldots, \quad (2.43)$$

intensities of which are given by

$$I_j^{\mathrm{PES}} \propto \left|\alpha_0^0\beta_0^j+\int_{-W/2}^{W/2}d\varepsilon\,\alpha_1^0(\varepsilon)\beta_1^j(\varepsilon)+\ldots\right|^2 . \quad (2.44)$$

The final states of the inverse photoemission or the wave functions of the $(N$+1)-electron system are expressed as

$$|E_j(N+1)\rangle=\gamma_0^j|d^{n+1}\rangle+\int_{-W/2}^{W/2}d\varepsilon\,\gamma_1^j(\varepsilon)|d^{n+2}\underline{L}(\varepsilon)\rangle+\int_{-W/2}^{W/2}d\varepsilon d\varepsilon'\,\gamma_2^j(\varepsilon,\varepsilon')|d^{n+3}\underline{L}(\varepsilon)\underline{L}(\varepsilon')\rangle+\ldots, \quad (2.45)$$

the intensities of which are given by

$$I_j^{\mathrm{PES}} \propto \left|\alpha_0^0\gamma_0^j+\int_{-W/2}^{W/2}d\varepsilon\,\alpha_1^0(\varepsilon)\gamma_1^j(\varepsilon)+\ldots\right|^2 . \quad (2.46)$$

## 2.4. Hartree-Fock band-structure calculation and self-energy correction

In order to investigate the effect of the translational symmetry of the 3*d* transition-metal ions beyond the cluster or Anderson single-impurity model, we have to study the Anderson lattice model. Since it is almost impossible to obtain the exact solutions of lattice models in the presence of strong electron-electron interaction, one has to employ certain approximations. The Hartree-Fock (HF) approximation is one of the most straightforward and well-defined approximation. In the case of integer band filling, it correctly gives the *d* bands which are split into upper and lower Hubbard bands for strong electron-electron interaction. If we have applied the HF approximation to the Anderson lattice model, the Hamiltonian $H_d$ is reduced to the mean-field Hamiltonian,

$$H_d^{MF} = \varepsilon_d^0 \sum_{i,m\sigma} d_{i,m\sigma}^+ d_{i,m\sigma} + \sum_{i,m\sigma,m'\sigma'} h_{m\sigma,m'\sigma'} d_{i,m\sigma}^+ d_{i,m'\sigma'}$$
$$+ \sum_{i,m\sigma,m'\sigma',m''\sigma'',m'''\sigma'''} U_{m\sigma,m'\sigma',m''\sigma'',m'''\sigma'''} \left\langle d_{i,m\sigma}^+ d_{i,m'\sigma'} \right\rangle d_{i,m''\sigma''}^+ d_{i,m'''\sigma'''}$$
$$+ \sum_{i,m\sigma,m'\sigma',m''\sigma'',m'''\sigma'''} U_{m\sigma,m'\sigma',m''\sigma'',m'''\sigma'''} d_{i,m\sigma}^+ d_{i,m'\sigma'} \left\langle d_{i,m''\sigma''}^+ d_{i,m'''\sigma'''} \right\rangle$$
$$- \sum_{i,m\sigma,m'\sigma',m''\sigma'',m'''\sigma'''} U_{m\sigma,m'\sigma',m''\sigma'',m'''\sigma'''} \left\langle d_{i,m\sigma}^+ d_{i,m'\sigma'} \right\rangle \left\langle d_{i,m''\sigma''}^+ d_{i,m'''\sigma'''} \right\rangle . \quad (2.47)$$

By solving the HF equations self-consistently, single-electron wave functions are obtained. The wave function of the ground state is written as a single Slater determinant constructed from the single-electron Bolch states. By means of Koopmans' theorem, the energy distribution of the ground-state single-electron states is regarded as a single-electron excitation spectrum. However, this assumption is not valid in many cases.

Starting from the HF solution, we can perform a perturbation expansion with respect to the Coulomb terms in order to investigate correlation effect beyond the HF approximation. Using the Heisenberg equation of motion for operators $A$ and $B$, $z << A; B >> = <[A, B]_+> + <<[A, H]_-; B>>$, the Green function satisfies

$$\omega G_{\tilde{k},\sigma}^R(\omega) = 1 + (\varepsilon_{\tilde{k},\sigma}^{HF} - \mu) G_{\tilde{k},\sigma}^R(\omega) - i\int_0^\infty <E_0(N)|[[a_{\tilde{k},\sigma}, H]_-, a_{\tilde{k},\sigma}^+]_+|E_0(N)> e^{i\omega t - \eta t} dt ,$$
$$\eta \to +0 , \quad (2.48)$$

where $\mu$ is Fermi level and $\varepsilon_{\tilde{k},\sigma}^{HF}$ are the Hartree-Fock energy levels. If we define the self-energy by



$$-i\int_0^\infty <E_0(N)|[[a_{\tilde{k},\sigma}, H]_-, a_{\tilde{k},\sigma}^+]_+|E_0(N)> e^{i\omega t - \eta t} dt \equiv \Sigma_{\tilde{k},\sigma}(\omega) G_{\tilde{k},\sigma}^R(\omega) , \quad (2.49)$$

the retarded Green's function is expressed as

$$G_{\tilde{k},\sigma}^R(\omega) = \frac{1}{\omega - (\varepsilon_{\tilde{k},\sigma}^{HF} - \mu) - \Sigma_{\tilde{k},\sigma}(\omega)} . \quad (2.50)$$

Therefore, by calculating the self-energy, one can obtain the single-electron excitation spectra through the relation (2.9). If the self-energy is expanded around the redefined Fermi level $\mu^*$, namely,

$$\Sigma_{\tilde{k},\sigma}(\omega) = \Sigma_{\tilde{k},\sigma}(\mu^*) + \left.\frac{\partial \Sigma_{\tilde{k},\sigma}(\omega)}{\partial \omega}\right|_{\omega=\mu^*} (\omega - \mu^*) + \cdots , \quad (2.51)$$

the retarded Green's function near the Fermi level is given by

$$G_{\tilde{k},\sigma}^R(\omega) = \frac{z_{\tilde{k},\sigma}}{\omega - (\varepsilon_{\tilde{k},\sigma}^* - \mu^*) - i\eta_{\tilde{k},\sigma}} , \quad (2.52)$$

where the renormalization constant or weight of the coherent part is expressed as

$$z_{\tilde{k},\sigma} = \left| 1 - \left.\frac{\partial \,\mathrm{Re}\, \Sigma_{\tilde{k},\sigma}(\omega)}{\partial \omega}\right|_{\omega=\mu^*} \right|^{-1} . \quad (2.53)$$

and $\varepsilon_{\tilde{k},\sigma}^*$ is the quasi-particle energy. $\eta_{\tilde{k},\sigma}$ vanishes as $(\omega - \mu^*)^2$ as $\omega \to \mu^*$. In the single-particle excitation spectrum, the intensity of the quasi-particle state near the Fermi level is multiplied by the renormalization constant which is derived from the frequency dependence of the self-energy. On the other hand, the effective mass can be defined in terms of the quasi-particle density of states at the Fermi level. The effective mass $m^*$ is expressed as the product of $\omega$-mass $m_\omega$ and $k$-mass $m_k$, which are defined by

$$\frac{m_\omega}{m} = \left| 1 - \left.\frac{\partial \,\mathrm{Re}\, \Sigma_{\tilde{k},\sigma}(\omega)}{\partial \omega}\right|_{\omega=\mu^*} \right|_{FS} , \quad (2.54)$$

and

$$\frac{m_k}{m} = \frac{\left|\frac{\partial \varepsilon^{HF}_{\vec{k},\sigma}}{\partial \vec{k}}\right|_{FS}}{\left|\frac{\partial \varepsilon^{HF}_{\vec{k},\sigma}}{\partial \vec{k}} + \frac{\partial \,\mathrm{Re}\,\Sigma_{\vec{k},\sigma}(\mu^*)}{\partial \vec{k}}\right|_{FS}}, \quad (2.55)$$

respectively [Mahan, 1981; Greeff *et al.*, 1992]. FS represents that the above formula is evaluated on the Fermi surface.



# Chapter three

# Electronic structure of $PrNiO_3$ studied by photoemission and x-ray absorption spectroscopy

The electronic structure of $PrNiO_3$ has been studied by photoemission and x-ray absorption spectroscopy. By analyzing the spectra using configuration-interaction calculations on a $NiO_6$ cluster model, it has been found that the charge-transfer energy $\Delta$ is ~ 1 eV and that the Ni 3*d* and O 2*p* orbitals are strongly hybridized in the ground state. From the cluster-model calculation, the magnetic moment of Ni 3*d* is estimated to be ~ 0.9 $\mu_B$, which is close to the ionic value of $Ni^{3+}$ and in good agreement with that obtained from neutron diffraction experiment. Using the electronic-structure parameters deduced from the cluster-model analysis, we have performed unrestricted Hartree-Fock calculations on a Ni 3*d*-O 2*p* perovskite-type lattice model in order to study the effect of $GdFeO_3$-type distortion on the orbital ordering and band gap.

## 3.1. Introduction

Perovskite-type 3*d* transition-metal oxides, which exhibit various physical properties, are very fascinating systems. One of them $R$NiO$_3$ ($R$=rare earth) shows a metal-insulator transition as a function of the size of the rare-earth ion or of the Ni-O-Ni bond angle. While the least distorted $LaNiO_3$, which has the rhombohedral structure, is a paramagnetic (PM) metal [Goodenough and Raccah, 1965], more distorted $R$NiO$_3$ with a smaller $R$ ion than La has the orthorhombic $GdFeO_3$-type structure (Fig. 3.1) and becomes an antiferromagnetic (AFM) insulator [Lacorre *et al.*, 1992; Torrance *et al.*, 1992; García-Muñoz *et al.*, 1992a]. Some orthorhombic $R$NiO$_3$ with an $R$ ion of intermediate size show metal-insulator transition as a function of temperature. The transition temperature increases as the $R$ ion becomes smaller [Lacorre *et al.*, 1992; Torrance *et al.*, 1992; García-Muñoz *et al.*, 1992a]. In addition to the metallic versus insulating behavior, the magnetic structures of AFM $PrNiO_3$ and $NdNiO_3$ were found to be very complicated and to indicate the existence of orbital ordering [García-Muñoz *et al.*, 1992b]. In order to reveal the origin of the electrical and magnetic properties of $R$NiO$_3$, it is very important to investigate its electronic structure.

The electronic structures of the 3*d* transition-metal compounds have been interpreted in the framework of the Zaanen-Sawatzky-Allen (ZSA) scheme [Zaanen *et al.*, 1985; Hüfner, 1985], where the transition-metal compounds are classified into two regimes, namely, the Mott-Hubbard regime and the charge-transfer regime. In the Mott-Hubbard regime, the 3*d*-3*d* Coulomb repulsion energy $U$ is smaller than the ligand-to-metal charge-transfer energy $\Delta$ and the magnitude of the band gap is given by $\sim U$. In the charge-transfer regime, where $\Delta < U$, the magnitude of the gap is determined by $\Delta$. Recently, it has been pointed out that the electronic structures of high valence oxides such as $Cu^{3+}$, $Ni^{3+}$ and $Fe^{4+}$ oxides are characterized by a small or even negative charge-transfer energy and the magnitude of the band gap is determined by the transition-metal 3*d*-oxygen 2*p* hybridization and hence is strongly affected by the geometrical arrangement of the transition-metal and oxygen ions [Mizokawa *et al.*, 1991; Bocquet *et al.*, 1992a; Sarma *et al.*, 1992]. In these compounds, therefore, a small lattice distortion may cause a metal-insulator transition.

$R$NiO$_3$ is a candidate for this kind of compounds and some studies have been done trying to understand its electronic structure. From neutron diffraction measurements on $PrNiO_3$ and $NdNiO_3$, García-Muños, Rodríguez-Carvajal and Laccorre [1992b] have shown that the ordered magnetic moment at the Ni site is $\sim 0.9\ \mu_B$, which is close to the purely ionic value 1 $\mu_B$ of $Ni^{3+}$ and has been taken as evidence for the ionic character of $R$NiO$_3$. Medarde *et al.* [1992] have performed x-ray-absorption spectroscopy (XAS) of $R$NiO$_3$ and have also concluded that the ground state has mainly $d^7$ character. Very recently, Barman, Chainani and Sarma [1994] have reported the photoemission spectroscopy study of $LaNiO_3$ and $NdNiO_3$. They claimed that the difference between the metallic $LaNiO_3$ and the insulating $NdNiO_3$ is



driven by the difference in the transition-metal 3*d*-to-oxygen 2*p* transfer integrals within the $NiO_6$ cluster. In this chapter, we have investigated the electronic structure of $PrNiO_3$ using photoemission and XAS measurement and subsequent cluster-model calculations. It has been found that the $d^7$ and $d^8\underline{L}$ configurations are strongly mixed in the ground state and that it does not contradict the magnetic moment close to the ionic value. Unrestricted Hartree-Fock (HF) calculations have also been performed on a Ni 3*d*-O 2*p* perovskite-type lattice model using the electronic-structure parameters deduced from the cluster-model analysis in order to investigate the relationship between the $GdFeO_3$-type lattice distortion and the metal-insulator transition of $R$NiO$_3$. It has been shown that the $GdFeO_3$-type distortion increases the magnitude of the band gap of $R$NiO$_3$.

The organization of this chapter is as follows. Experimental details are presented in Sec. 3.2. The methods of the cluster-model and unrestricted HF calculations are described in Sec. 3.3. In Sec. 3.4, photoemission spectra and XAS spectra are displayed and are analyzed by the calculations.

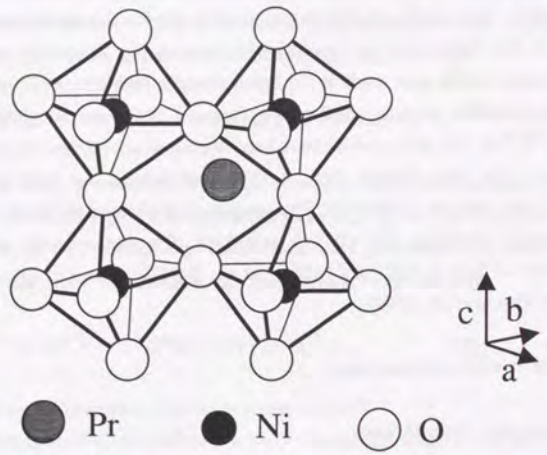


**Fig. 3.1.** Simplified structure of the $GdFeO_3$-type lattice. The Ni-O-Ni bond angle decreases from 180° as the distortion increases.

### 3.2. Experimental

Polycrystalline samples of $PrNiO_3$ were supplied by Prof. Tokura's group in University of Tokyo. The starting material was prepared by dissolving $Pr_6O_{11}$ and NiO in concentrated nitric acid. The excess nitric acid was removed by heating it to 200 °C in air. The remaining intimately mixed nitrates were decomposed to black powders at 800 °C in an $O_2$ atmosphere. After grinding, the powders were sealed in a platinum capsule with $KClO_3$ and pressurized under 5 GPa using a cubic anvil high pressure apparatus. Heat treatment under pressure was carried out at 1300 °C for an hour [Arima *et al.*, 1993].

Photoelectrons were collected with a Physical Electronics double-pass cylindrical-mirror analyzer both for x-ray photoemission spectroscopy (XPS) and ultra-violet photoemission spectroscopy (UPS). A Mg Kα x-ray source ($h\nu$=1253.6 eV) was used for the XPS measurements. The XPS spectra were corrected for the Mg $K\alpha_{3,4}$ ghost. The energy resolution including both the x-ray source and the analyzer was ~ 1.0 eV. The binding energy in XPS was calibrated using the Au $4f_{7/2}$ peak at 84.0 eV [Hüfner, 1995]. UPS spectra were measured at beamline BL-2 of Synchrotron Radiation Laboratory, Institute for Solid State Physics, University of Tokyo. The energy resolution was 0.3-0.5 eV for the photon energy ranging from 40 to 100 eV. The Fermi level was determined by evaporating Au on the sample. All the photoemission measurements were made at the liquid-nitrogen temperature. In order to obtain fresh surfaces, the samples were scraped with a diamond file under an ultrahigh vacuum (UHV) of low $10^{-10}$-Torr. The XAS spectra have been measured at beamline BL-2B of Photon Factory, Laboratory for High Energy Physics. The measurement has been done at room temperature in the total electron yield mode. The samples were scraped under an UHV of low $10^{-9}$ Torr. The energy resolution was ~ 0.2 eV at 530 eV. The photon energy was calibrated using the O 1*s* edge of $TiO_2$ at 530.7 eV [Abbate *et al.*, 1992] and the Cu $2p_{3/2}$ edge of Cu metal at 932.5 eV [Grioni *et al.*, 1989].

### 3.3. Methods of model calculations

#### 3.3.1. Cluster-model calculations

We have analyzed the photoemission and x-ray absorption spectra using configuration-interaction (CI) calculations on an octahedral $NiO_6$ cluster model (with $O_h$ symmetry) [Fujimori and Minami, 1984]. The wave functions for the cluster are spanned by basis functions of the ionic configuration $d^n$ and the charge-transferred configurations $d^{n+m}\underline{L}^m$, where $\underline{L}$ denotes an oxygen 2*p* hole. The wave function of the ground state or the *N*-electron system is given by

$$|E_0(N)> = a_0|d^7> + a_1|d^8\underline{L}> + a_2|d^9\underline{L}^2> . \qquad (3.1)$$



The oxygen 2*p*-to Ni 3*d* charge-transfer energy is defined by $\Delta \equiv E(d^8\underline{L}) - E(d^7)$ and the 3*d*-3*d* Coulomb interaction energy by $U \equiv E(d^6) + E(d^8) - 2E(d^7)$, where $E(d^n\underline{L}^m)$ is the center of gravity of the $d^n\underline{L}^m$ multiplets or the average of all the terms in the multiplets including the degeneracies. The final states of 3*d* photoemission or the (*N*-1)-electron states, are expressed by

$$|E(N\text{-}1)> = b_0|d^6> + b_1|d^7\underline{L}> + b_2|d^8\underline{L}^2> . \qquad (3.2)$$

The energy differences $E(d^7\underline{L}) - E(d^6)$ and $E(d^8\underline{L}^2) - E(d^7\underline{L})$ are $\Delta - U$ and $\Delta$, respectively. Corresponding 3*d* photoemission intensities are given by $|a_0b_0 + a_1b_1 + a_2b_2|^2$ in the sudden approximation. In the same way, the wave function of the (*N*+1)-electron states are written as

$$|E(N+1)> = c_0|d^8> + c_1|d^9\underline{L}> + c_2|d^{10}\underline{L}^2> . \qquad (3.3)$$

These can be regarded as the final states of O 1*s* XAS if we neglect interaction between an O 1*s* core hole and Ni 3*d* electrons. Their intensities are proportional to $|a_1c_0 + a_2c_1|^2$.

The final states of Ni 2*p* core-level photoemission are given by

$$|E^c(N)> = d_0|\underline{c}d^7> + d_1|\underline{c}d^8\underline{L}> + d_2|\underline{c}d^9\underline{L}^2> + d_3|\underline{c}d^{10}\underline{L}^3> , \qquad (3.4)$$

where $\underline{c}$ denotes a Ni 2*p* core hole. When the Coulomb interaction between a Ni 2*p* hole and a Ni 3*d* hole is denoted by *Q*, the energy differences $E(\underline{c}d^8\underline{L}) - E(\underline{c}d^7)$ and $E(\underline{c}d^9\underline{L}^2) - E(\underline{c}d^8\underline{L})$ are $\Delta - Q$ and $\Delta - Q + U$, respectively. The 2*p* core-level photoemission intensities are given by $|a_0d_0 + a_1d_1 + a_2d_2|^2$. For Ni 2*p* XAS, the final states are expressed by

$$|E^c(N+1)> = e_0|\underline{c}d^8> + e_1|\underline{c}d^9\underline{L}> + e_2|\underline{c}d^{10}\underline{L}^2> , \qquad (3.5)$$

whose intensities are proportional to $|a_0e_0 + a_1e_1 + a_2e_2|^2$.

In the cluster-model calculations for the valence-band spectra, we have three adjustable parameters which are to be determined to reproduce the experimental results: $\Delta$, $U$ and the transfer integrals between the Ni 3*d* and O 2*p* orbitals. The transfer integrals are expressed in terms of Slater-Koster parameters ($pd\sigma$) and ($pd\pi$) [Slater and Koster, 1954]. The ratio ($pd\sigma$)/($pd\pi$) is fixed to be ~-2.2 [Mattheiss, 1972; Harrison, 1989] and only ($pd\sigma$) is taken as an adjustable parameter. The multiplet splitting of $d^n$ configurations are taken into account through Racah parameters, *B* and *C*, which have been fixed to the free-ion values [Sugano *et al.*, 1970; Mann]. The multiplet-averaged 3*d*-3*d* Coulomb interaction *U* and charge-transfer energy $\Delta$ for $d^n$ are given by $A - 14/9B + 7/9C$ and $\varepsilon_d^0 - \varepsilon_p + nU$, respectively, where $\varepsilon_d^0$ and

$\varepsilon_p$ are the bare energy levels of the 3*d* and 2*p* orbitals. For the Ni 2*p* core-level spectra, the Coulomb interaction between the Ni 2*p* hole and the Ni 3*d* hole *Q* is added to the above three adjustable parameters. From previous cluster-model analyses, it has empirically been found that the ratio *U*/*Q* should be 0.7-0.9 [Zaanen *et al.*, 1986; Okada and Kotani, 1991; Bocquet *et al.*, 1992b]. In the present calculation, the ratio *U*/*Q* is assumed to be 0.8. When we tentatively varied the ratio within the above range, agreement with experimental results were not improved significantly. The multiplet coupling between the Ni 2*p* core hole and the Ni 3*d* holes is included through Slater integrals $F^2$, $G^1$ and $G^3$, which are also fixed to the free-ion values [Mann; de Groot *et al.*, 1990].

We have included the crystal-field splitting 10*Dq* which arises from the non-orthogonality between the atomic oxygen 2*p* and transition-metal 3*d* orbitals [Harrison, 1989]. The overlap integrals can be deduced from the linear-combination-of-atomic-orbitals (LCAO) fitting of the band-structure calculations by Mattheiss [1972]. We have assumed the ratio of the overlap integrals $S_\sigma$ and $S_\pi$ to the transfer integrals $(pd\sigma)$ and $(pd\pi)$ to be ~ -0.06 $eV^{-1}$. The 10*Dq* from the non-orthogonality is given by $-2(V_e S_e - V_{t2} S_{t2})$, where $V_e = -\sqrt{3}(pd\sigma)$, $S_e = -\sqrt{3}S_\sigma$ and $V_{t2} = 2(pd\pi)$, $S_{t2} = 2S_\pi$.

In general, it is hard to reproduce both the valence-band and core-level photoemission spectra using the same parameter set in the cluster-model calculations because the final states have different numbers of 3*d* electrons and core hole. In this work, configuration dependence of the transfer integrals has been taken into account to make it possible to reproduce the valence-band and Ni 2*p* core-level XPS spectra with the same parameter set. Following Gunnarsson and Jepsen [1988], we have assumed that the transfer integrals between $d^{n-1}\underline{L}^m$ and $d^n\underline{L}^{m+1}$ are 80% of those between $d^n\underline{L}^m$ and $d^{n+1}\underline{L}^{m+1}$ and that those between $\underline{c}d^n\underline{L}^m$ and $\underline{c}d^{n+1}\underline{L}^{m+1}$ are 70% of those between $d^n\underline{L}^m$ and $d^{n+1}\underline{L}^{m+1}$.

### 3.3.2. Unrestricted Hartree-Fock calculations

In order to study the effect of translational symmetry, we have performed unrestricted HF calculations on the perovskite-type Ni 3*d*-O 2*p* lattice. The unrestricted HF approximation is a powerful tool to study spin and orbital-ordered insulating states in the lattice model. Cyrot and Lyon-Caen [1975] have made HF calculation on a doubly-degenerate Hubbard model and found that the ferromagnetic (FM) state with orbital ordering is favored. Recently, the HF calculations have been made for the $CuO_2$ plane, where there is no degeneracy in the 3*d* orbital, to study the metal-insulator boundary in the ZSA diagram [Nimkar *et al.*, 1993]. This study has shown that the HF approximation is useful to investigate metal-insulator transitions.

In our model, the intra-atomic 3*d*-3*d* Coulomb interaction is taken into account in terms of Kanamori parameters, *u*, *u'*, *j* and *j'*, for which the relationships $u' = u - 2j$ and $j' = j$ are assumed [Kanamori, 1963]. These Kanamori parameters can be related to Racah parameters



through $u = A + 4B + 3C$ and $j = (5/2)B + C$. The multiplet-averaged 3*d*-3*d* Coulomb interaction *U* and charge-transfer energy Δ for the $d^n$ configuration are given by $u - (20/9)j$ and $\varepsilon_d^0 - \varepsilon_p + nU$.

Our criterion for the self-consistency of the HF calculation is that all the differences of the order parameters in the subsequent iteration steps are less than $1 \times 10^{-3}$. We have taken 512 **k**-points in the first Brillouin zone for the $GdFeO_3$ structure, whose unit cell has four Ni sites, and 64 **k**-points for the actual magnetic structure of $PrNiO_3$, whose unit cell contains 16 Ni sites. In the present calculations, the $GdFeO_3$-type distortion of $PrNiO_3$ is imitated by rotating the $NiO_6$ octahedra of the cubic perovskite structure around the *a*-axis of the $GdFeO_3$ structure (see Fig. 3.1).

## 3.4. Results and discussion

### 3.4.1. Core-level XPS

In Fig. 3.2, we have plotted the XPS spectrum of the O 1*s* core level which overlaps with the Pr MNN Auger spectrum. The O 1*s* peak at 528.3 eV is almost a single peak, which shows the cleanness of the surface. The broad structure at ~ 531 eV may be derived from surface contaminations superposed on the Pr MNN emission. The amount of the contamination is small enough for us to analyze the following spectra and to extract information on the electronic structure of $PrNiO_3$.

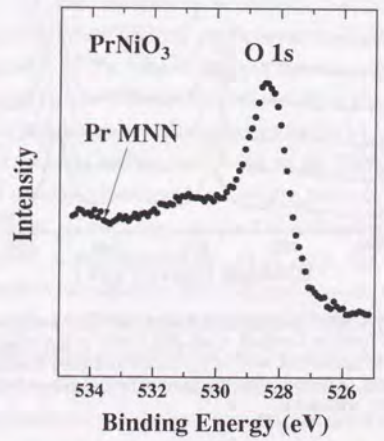


**Fig. 3.2.** O 1*s* XPS spectrum of $PrNiO_3$. The spectrum has been corrected for the Mg $K\alpha_{3,4}$ satellites.

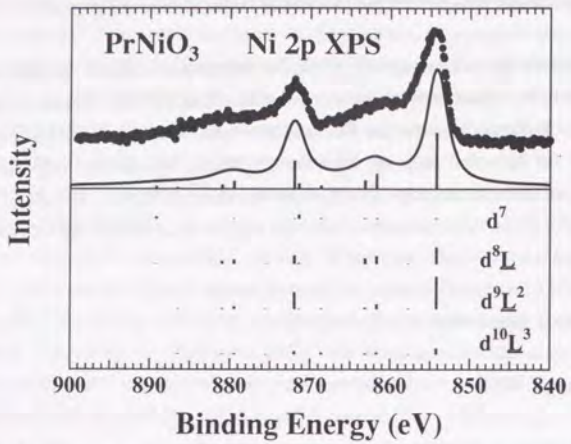


**Fig. 3.3.** Ni 2*p* XPS spectrum of $PrNiO_3$ compared with the cluster-model calculation without multiplet coupling (upper panel). The line spectra are decomposed into the $d^7$, $d^8\underline{L}$, $d^9\underline{L}^2$ and $d^{10}\underline{L}^3$ components (lower panel).

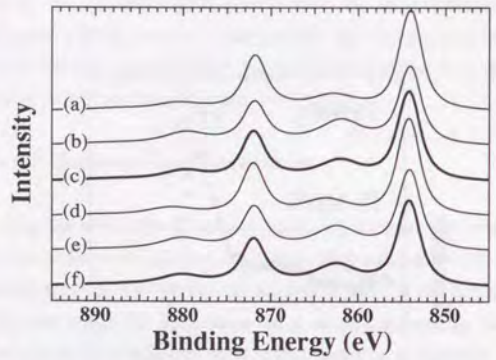


**Fig. 3.4.** Ni 2*p* XPS spectra calculated without $d^{10}\underline{L}^3$ configuration both in the initial and final states (curves a and d), with $d^{10}\underline{L}^3$ only in the initial states (curves b and e), with $d^{10}\underline{L}^3$ configurations both in the initial and final states (curves c and f). Curves a, b and c were obtained with the configuration dependence of the transfer integrals and the others without it.



As shown in Fig. 3.3, the Ni 2*p* core-level XPS spectrum has satellite structures, which have been generally observed in late transition-metal oxides. We have analyzed the Ni 2*p* core-level spectrum using the CI cluster model with and without multiplet effect. The Ni 2*p* spectrum calculated without the multiplet effect are compared with the experimental results in the upper panel of Fig. 3.3. Here, we have broadened the line spectra by a Lorentzian, the full width at half maximum (FWHM) of which is proportional to the energy separation from the main peak [Bocquet *et al.*, 1992b]. In calculating the Ni 2*p* core-level spectrum, $Q$ is assumed to be $\sim U/0.8$. With $U$ and $Q$ being fixed at 7 eV and 9 eV, respectively, the best fit has been obtained for $\Delta = 1 \pm 1$ eV and $(pd\sigma) = -1.5 \pm 0.2$ eV. The final states are decomposed into $\underline{c}d^7$, $\underline{c}d^8\underline{L}$, $\underline{c}d^9\underline{L}^2$ and $\underline{c}d^{10}\underline{L}^3$ components in the lower panel of Fig. 3.3. The main peaks and the satellite structures have $\underline{c}d^9\underline{L}^2$ and $\underline{c}d^8\underline{L}$ character, respectively. The amount of $d^{10}\underline{L}^3$ in the main peak is not negligible since $\Delta$ is smaller than $Q$-$U$ in the present calculation.

Here, we have investigated the effect of neglecting the $d^{10}\underline{L}^3$ configuration in the final state of the Ni 2*p* XPS. In Fig. 3.4, we have plotted the calculated results (a) without the $d^{10}\underline{L}^3$ configuration both in the initial and final states, (b) without the $d^{10}\underline{L}^3$ configuration only in the final states, (c) with the $d^{10}\underline{L}^3$ configuration both in the initial and final states. As expected, neglecting the $d^{10}\underline{L}^3$ configuration in the initial state is not serious. However, the lack of $d^{10}\underline{L}^3$ in the final states strongly affects the calculated spectra and would prevent us from estimating the parameters accurately. The three calculations have been done including the configuration dependence of the transfer integrals [Gunnarsson and Jepsen, 1988]. The failure of neglecting $d^{10}\underline{L}^3$ might be enhanced by the inclusion of the configuration dependence. Therefore we have also done the above three calculations without the configuration dependence, which are shown in (d), (e) and (f) of Fig. 3.4. The configuration dependence does not so drastically change the spectrum. This is because the relative intensity and the separation between the main and satellite peaks are mainly determined by the transfer integral between $\underline{c}d^8\underline{L}$ and $\underline{c}d^9\underline{L}^2$, where the transfer integrals are almost equal to those between $d^7$ and $d^8\underline{L}$ in the ground state.

We have also performed cluster-model calculations for the Ni 2*p* spectrum by fully taking the intra-atomic multiplet coupling into account. When all the configurations up to $d^{10}\underline{L}^3$ are included, the number of basis becomes very large (6820). Since numerical diagonalization of such a large matrix is difficult, we have employed the Lanczos method [Gagliano and Balseiro, 1988]. However the amount of the calaulation is still so huge that we could not do iterative calculations to find the best-fit parameter set. Here, we have done the calculation using the same parameter set as that obtained without the multiplet effect. Since the satellite structures are broadened by the multiplet splittings, there is no need to apply the extra broadening for the satellite part although the inclusion of a weak Lorentzian broadening somewhat improves agreement between experiment and calculation. The calculated result using $\Delta = 1$ eV, $U = 7$ eV and $(pd\sigma) = -1.5$ eV is compared with the experimental result in Fig. 3.5. The Slater integrals between the Ni 2*p* and 3*d* orbitals are $F^2 = 6.68$, $G^1 = 5.07$, $G^3 = 2.88$ eV [Mann; de Groot *et*

*al.*, 1990; Okada and Kotani, 1991]. The multiplet-averaged 2*p*-3*d* Coulomb interaction $Q$ [$\equiv F^0 - (1/15)G^1 - (3/70)G^3$] is ~ 9.0 eV. The Racah parameters $B$ and $C$ are fixed at 0.142 and 0.527 eV, which are 80% of the atomic HF values [Mann; de Groot *et al.*, 1990; Okada and Kotani, 1991]. Although the value of $B$ and $C$ are slightly different from those obtained from atomic spectroscopy data [Sugano *et al.*, 1970; Griffith, 1971], the differences do not affect the present conclusion. The crystal field from the non-orthogonality is ~ 0.57 eV for the ground state. The Pr 3*d* core-level photoemission spectrum is very similar to that of $Pr_2O_3$ [Ogasawara *et al.*, 1991], which indicates that the valence of the Pr ion is exactly 3+. This confirms that the formal valence of Ni is 3+.

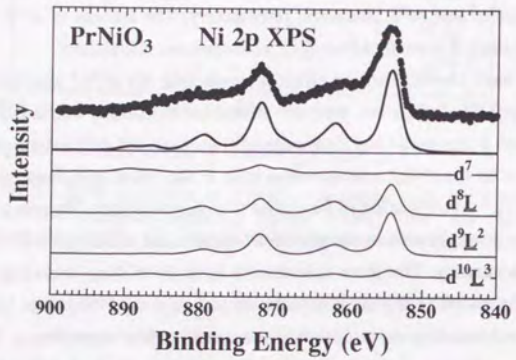


**Fig. 3.5.** Ni 2*p* XPS spectrum of $PrNiO_3$ compared with the cluster-model calculation with multiplet coupling (upper panel). The line spectra are decomposed into the $d^7$, $d^8\underline{L}$, $d^9\underline{L}^2$ and $d^{10}\underline{L}^3$ components (lower panel).

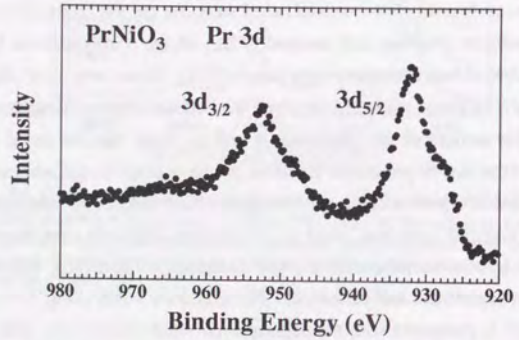


**Fig. 3.6.** Pr 3*d* XPS spectrum of $PrNiO_3$.



### 3.4.2. Valence band

The valence-band photoemission spectra taken at various photon energies from 40 eV to 1253.6 eV are shown in Fig. 3.7. Since the relative photoioization cross section of O 2*p* to Ni 3*d* and Pr 4*f* increases as the photon energy decreases, the structure at 5 eV is dominated by the O 2*p* character and the structure at 1.5 eV is mainly derived from the Ni 2*p* and Pr 4*f* states. In order to extract the Pr 4*f* contribution from the valence-band spectra, we have measured the Pr 4*d*-4*f* resonant-photoemission spectra (Fig. 3.8). By subtracting the off-resonant spectra ($h\nu$ = 120 eV) from the on-resonant ($h\nu$ =124 eV), we obtain the Pr 4*f*-derived spectrum as shown in Fig. 3.8. Here, we have assumed that the intensity distribution of the on-resonant Pr 4*f*-derived spectrum is not changed from that of the off-resonant spectrum.

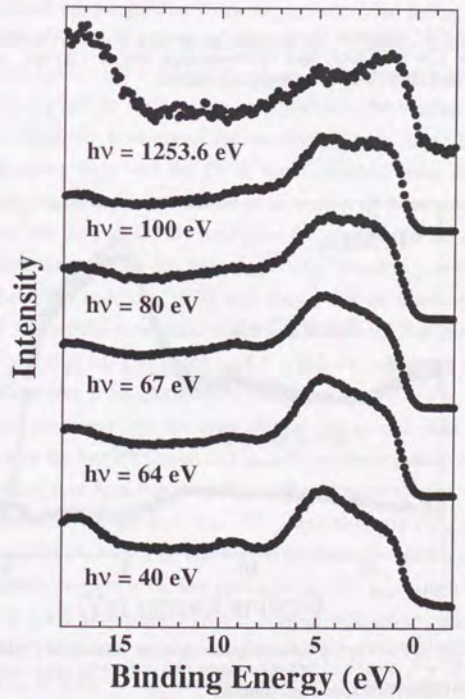


**Fig. 3.7.** Valence-band XPS and UPS spectra of $PrNiO_3$ taken at $h\nu$ = 40, 64, 67, 80, 100 and 1253.6 eV.

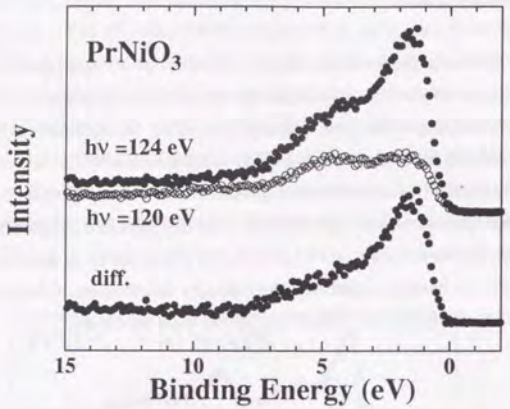


**Fig. 3.8.** Pr 4*d*-4*f* resonant photoemission spectra of $PrNiO_3$ taken with on-resonance ($h\nu$ = 124 eV, dots) and off-resonance ($h\nu$ = 120 eV, open circles) photon energies and their difference spectrum (dots).

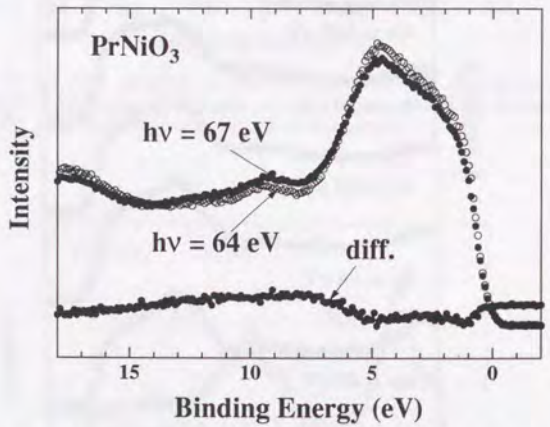


**Fig. 3.9.** Ni 3*p*-3*d* resonant photoemission spectra of $PrNiO_3$ taken with on-resonance ($h\nu$ = 67 eV, dots) and off-resonance ($h\nu$ = 64 eV, open circles) photon energies and their difference spectrum (dots).



Ni 3*p*-3*d* resonant-photoemission spectra have also been measured. The photon energy dependence of the monochrometer has been corrected using the photon absorption of Au taken in the total electron yield mode. As shown in Fig. 3.9, the broad satellite structure ranging from 7 eV to 15 eV is enhanced by the 3*p*-3*d* resonance and can be assigned to a so-called charge-transfer satellite. Intensity of the main-band region ranging from 0 eV to 5 eV is reduced from 64 eV to 67 eV because of the reduction of the photoionization cross section of O 2*p*. The weak structure at ~ 9.5 eV, which appears in the spectra taken at low photon energies ($h\nu$ = 40, 64 and 67 eV), would be from surface contamination.

In analyzing the valence-band XPS spectrum of $PrNiO_3$, we have performed a CI calculation on an octahedral $NiO_6^{9-}$ cluster model including multiplet coupling [Fujimori and Minami, 1984]. After subtracting the background due to secondary electrons, the existence of the broad satellite structure from 8 to 14 eV becomes clear. We have determined the value of $\Delta$, $U$ and $(pd\sigma)$ in order to reproduce the shape of the spectra including the satellite structure. The result of the CI calculation is compared with the experimental data in Fig. 3.10. The FWHM of the Gaussian is ~ 1.0 eV, which is mainly determined by the energy resolution of the analyzer, and that of the Lorentzian is ~ $0.4 + 0.3E_B$ eV, where the first term is derived from the natural width of the x-ray source and the second term proportional to the binding energy $E_B$ is from the life time of the final states. We have added the contribution from the O 2*p* band centered at ~5 eV assuming a Gaussian form and the Pr 4*f* band obtained from the Pr 4*d*-4*f* resonant photoemission taking into account the relative cross section of these atomic orbitals [Yeh and Lindau, 1985]. Here, we have artificially multiplied the photoionization cross section of the O 2*p* subshell by a factor three, which has been empirically found in previous studies. The XPS study of $V_2O_3$ by Sawatzky and Post [1979] also shows that the intensity ratios of O 2*p* to O 2*s* and of O 2*p* to V 3*d* are three time larger than those calculated. The best-fit parameters are $\Delta$ = 1.0 ± 1.0 eV, $U$ = 7.0 ± 1.0 eV, $(pd\sigma)$ = -1.5 ± 0.2 eV, which are consistent with those obtained from the Ni 2*p* core-level spectrum.

For the present parameter set, the symmetry of the ground state is found to be $^2E_g$, namely, the Ni ion is in the low-spin state. In Fig. 3.11, we have plotted the number of $d$ holes $N_d$ and the magnitude of spin $S_d$ as functions of $\Delta$. (The other parameters are fixed to the above values.) The boundary between the high-spin ($^4T_{1g}$) and low-spin ($^2E_g$) states is $\Delta$ ~ 2.0 eV. The ground state has 34% $d^7$, 56% $d^8\underline{L}$, and 10% $d^9\underline{L}^2$ characters and is strongly covalent. The calculated local magnetic moment in the low-spin state is 0.91 $\mu_B$, which is close to the purely ionic value and is in good agreement with the neutron diffraction measurement by García-Muñoz *et al.* [1992b]. The reason why the magnetic moment is close to the ionic value of the low-spin $Ni^{3+}$, 1 $\mu_B$, in spite of the strongly covalent ground state is as follows. Let us consider charge-transfer to the ionic low-spin configuration $t_{2g}\uparrow^3 t_{2g}\downarrow^3 e_g\uparrow$. The charge transfer of an electron whose spin is parallel to the Ni 3*d* local spin is more favored by the intra-atomic exchange interaction than that of an electron whose spin is antiparallel to the Ni spin. On the

other hand, for an electron with antiparallel spin, two $e_g$ orbitals are available for charge transfer while, for an electron with parallel spin, only one $e_g$ orbital is available. Since these two effects cancel each other, namely, the amount of the charge transfer for the parallel spin is almost equal to that for the antiparallel spin, the net local spin of Ni remains close to the purely ionic one. Actually, 26% of the ground state is of $t_{2g}\uparrow^3 t_{2g}\downarrow^3 e_g\uparrow^2 \underline{L}\uparrow$ type and 30 % is of $t_{2g}\uparrow^3 t_{2g}\downarrow^3 e_g\uparrow e_g\downarrow \underline{L}\downarrow$ type.

In the final state of the valence-band photoemission, $d^7\underline{L}$ character is dominant in the main band at 1.5 eV, and the satellite region has mainly $d^6$ and $d^8\underline{L}^2$ character. The $d^6$ character in satellite region causes the enhancement of the satellite intensity in the Ni 3*p*-3*d* resonant photoemission spectrum. The symmetry of the first ionization state is $^1A_{1g}$, which has 5% $d^6$, 53% $d^7\underline{L}$ and 42% $d^8\underline{L}^2$ characters. Using the same parameter set, the first affinity state with $^3A_{2g}$ symmetry is found to be dominated by $d^8$ character ( 84% $d^8$ and 16% $d^9\underline{L}$).

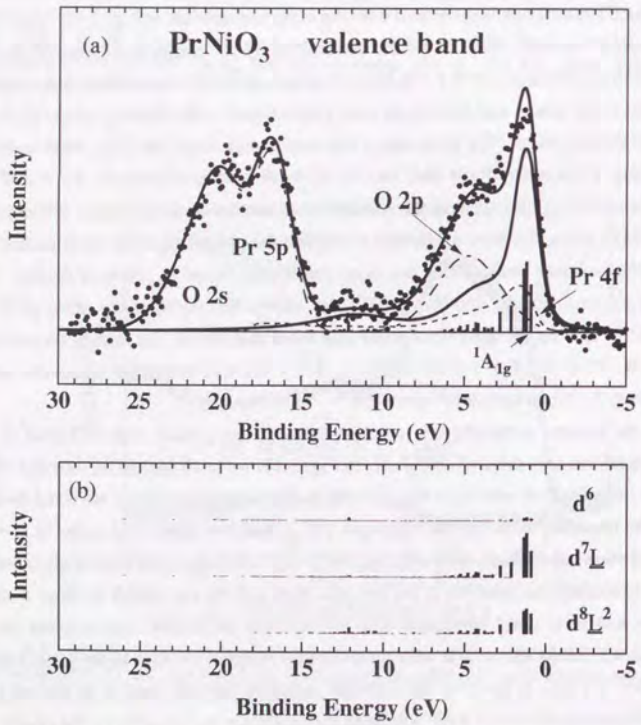


**Fig. 3.10.** (a) Cluster-model calculation for valence-band photoemission spectrum compared with the experimental result. (b) The line spectra are decomposed into the $d^7$, $d^8\underline{L}$ and $d^9\underline{L}^2$ components.



Here, let us consider the characters of the excitations from the ground state to the first ionization and affinity states. The *d* and *p* weights of the excitation from the ground state to the first ionization state are given by the differences between the net numbers of *d* and *p* holes in the ground state and those in the first ionization state, respectively. Those of the excitation from the ground state to the first affinity state are also given in the same way. In our cluster-model analysis, the net numbers of the *d* and *p* holes are 2.24 and 0.76 in the ground state, 2.63 and 1.37 in the first ionization state and 1.84 and 0.16 in the first affinity state, respectively. Therefore the excitation from the ground state to the first ionization state has 39% *d* and 61% *p* character and that from the ground state to the first affinity state has 40% *d* and 60% *p* character. Therefore, the band gap of ~ 2.3 eV obtained by the cluster-model calculation is far from being of *p-d* or charge-transfer type, but has strongly-hybridized "*pd-pd*" character.

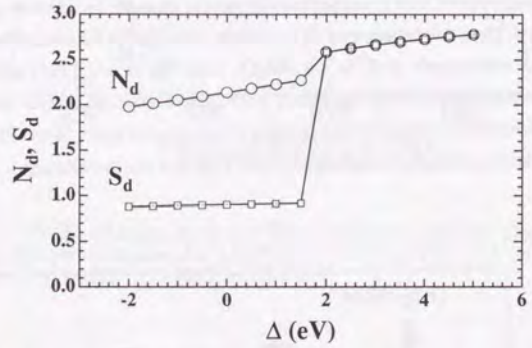


**Fig. 3.11.** Number of *d* holes $N_d$ and spin $S_d$ in the ground state of the $NiO_6$ cluster as functions of Δ. The parameters ($pd\sigma$) and *U* are fixed at -1.5 and 7.0 eV, respectively.

### 3.4.3. X-ray absorption spectra

An O 1*s* XAS spectrum reflects the O 2*p* weight hybridized into the unoccupied states of the transition-metal and rear-earth ions [de Groot *et al.*, 1989]. The O 1*s* spectrum of $PrNiO_3$ is shown in the Fig. 3.12, which is in good agreement with that measured by Medarde *et al.* [1992]. The sharp peak at 529 eV is derived from the Ni 3*d* state and the structures ranging from 530 eV to 545 eV are due to the Pr 4*f*, 5*d* and Ni 4*s*, 4*p* states. If we neglect the effect of the O 1*s* core-hole potential on the unoccupied states, the final state of the O 1*s* XAS can be regarded as the (*N*+1)-electron state, which is equivalent to the final state of inverse photoemission. We have calculated the O 1*s* XAS spectrum using the cluster model with the

above parameter set and have compared it with the experimental result in Fig. 3.12. Here, we have shifted the calculated O 1*s* XAS spectrum by 1.4 eV towards lower photon energy from the photon energy equal to O 1*s* binding energy in XPS. According to the calculation, the dominant peak is due to the first affinity level $^3A_{2g}$ and the high energy tail is derived from $^1E_g$ and $^1A_{1g}$ states.

In Fig. 3.13, we have compared the Ni 2*p* XAS spectrum with the full-multiplet cluster-model calculation, which has been obtained by broadening the line spectrum with a Gaussian and a Lorentzian. The FWHM of the Gaussian is ~ 0.6 eV, which is determined by the energy resolution, and that of the Lorentzian is ~ 0.5 eV, which is derived from the natural width [Krause and Oliver, 1979]. The parameters used in this calculation are exactly the same as those for the Ni 2*p* XPS spectra. It has been shown that the double-peak structure of the $2p_{3/2}$ main peak is due to the multiplet splitting. Weak and broad satellite structures, which are located on the high energy side separated by ~ 5 eV from the main peak, are reproduced to some extent. In order to improve agreement with the experimental results, an extra broadening of the calculated result is necessary. The extra broadening of transition-metal 2*p* XAS has also been observed in the mixed valence compounds such as $Li_{1-x}Ni_xO_2$ [van Elp *et al.*, 1991] and $La_{1-x}Sr_xFeO_3$ [Abbate *et al.*, 1992] and has been attributed to the coexistence of several components with different symmetries (in the single-cluster picture) in the ground state. Since $PrNiO_3$ is located at the metal-insulator boundary, it may undergo this type of extra broadening.

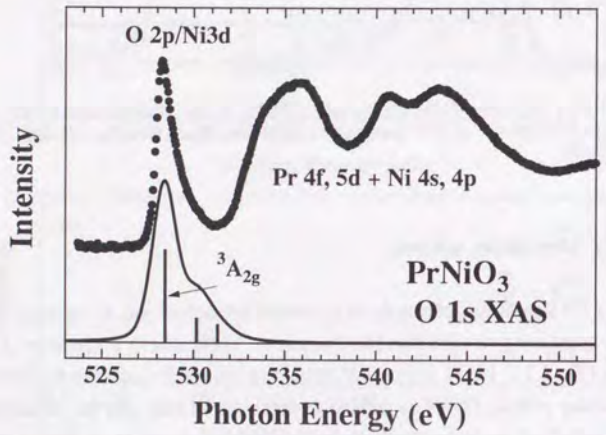


**Fig. 3.12.** O 1*s* XAS spectrum of $PrNiO_3$ compared with the cluster-model calculation. The parameters are $\Delta = 1.0$ eV, $U = 7.0$ eV and $(pd\sigma) = -1.5$ eV.



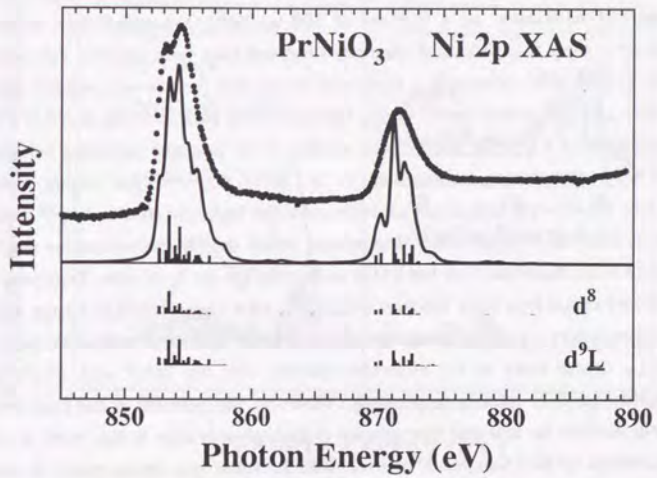


**Fig. 3.13.** Ni 2*p* XAS spectrum of $PrNiO_3$ compared with the cluster-model calculation. The parameters are $\Delta = 1.0$ eV, $U = 7.0$ eV, $(pd\sigma) = -1.5$ eV and $F^0 = 9.5$ eV. $Q \equiv F^0 - (1/15)G^1 - (3/70)G^3 \approx 9.0$ eV.

### 3.4.4. Unrestricted Hartree-Fock calculations

From the above cluster-model calculations, it has been found that $PrNiO_3$ has a small positive $\Delta \sim 1$ eV and that the $d^7$ and $d^8\underline{L}$ configurations are strongly hybridized in the ground state. In transition-metal oxides with very small positive or negative $\Delta$, the magnitude of the band gap is strongly affected by the geometrical arrangement of the transition-metal and oxygen ions. Actually, $RNiO_3$ shows a metal-to-insulator transition as a function of the size of the *R* ion, which controls the magnitude of the $GdFeO_3$-type lattice distortion. In order to investigate the relationship between the $GdFeO_3$-type distortion and the metal-to-insulator transition in $RNiO_3$, we have made unrestricted HF calculations on a perovskite-type lattice model.

The magnetic structure of $PrNiO_3$ has been found to be very complicated and to give a large unit cell containing 16 unit formulas. Each Ni spin is ferromagnetically coupled to three nearest neighbor Ni spins and antiferromagnetically coupled to the other three [García-Muñoz *et*

*al.*, 1992b]. In order to explain this unusual magnetic ordering, it has been proposed that the $e_g$ electrons of the low-spin $Ni^{3+}$ ($t_{2g}\uparrow^3 t_{2g}\downarrow^3 e_g\uparrow$) are polarized into the $3z^2$-$r^2$ and $x^2$-$y^2$ orbitals for the ferromagnetically coupled Ni pair and are polarized into one of these orbitals for the antiferromagnetically coupled Ni pair [García-Muñoz *et al.*, 1992b]. Since the magnetic structure can be viewed as a mixture of FM and *G*-, *A*- and *C*-type AFM magnetic arrangements, these four simplified magnetic structures have been studied. The high-spin state with the *G*-type AFM ordering has the lowest energy and the low-spin metallic state with the FM ordering has the second lowest energy for the realistic parameter set: $\Delta$ = 1.0 eV, $U$ = 7.0 eV and ($pd\sigma$) = -1.8 eV. The third lowest solution is the low-spin insulating solution with the *A*-type AFM arrangement accompanied by a "$3x^2$-$r^2$"/"$3y^2$-$r^2$"-type orbital ordering. The reason why the low-spin state is not so stabilized as the high-spin state in the HF approximation may be as follows. A single Slater determinant within the HF approximation can be a good description of the high-spin state but it fails to describe the low-spin state. Especially, for small $\Delta$, a Heitler-London type wave function $1/\sqrt{2}(|\underline{u}\uparrow\underline{L_u}\downarrow\underline{v}\uparrow| + |\underline{L_u}\uparrow\underline{u}\downarrow\underline{v}\uparrow|)$ has a large weight in the ground state, where $\underline{u}$ and $\underline{v}$ represent holes in the $3z^2$-$r^2$ and $x^2$-$y^2$ orbitals, respectively, and $\underline{L_u}$ and $\underline{L_v}$ denote holes in the molecular orbitals with the $3z^2$-$r^2$ and $x^2$-$y^2$ symmetries constructed from O 2*p* orbitals, respectively. Therefore, the inclusion of this kind of correlation effect will stabilize the low-spin state relative to the high-spin state. In this work, we have done HF calculations for the 16-molecule unit cell with the actual spin arrangement, in which the $e_g$ electrons are polarized into "$3z^2$-$r^2$" and "$x^2$-$y^2$" orbitals. The solution has an energy by ~ 50 meV/unit-formula higher than the *A*-type AFM solution. Further investigations would be required to understand why the complicated magnetic structure is realized in the low-spin $PrNiO_3$.

It is interesting to investigate how far the HF calculation can describe the photoemission spectra or the single-particle excitation spectra. In Fig. 3.14, the density of states for the *A*-type AFM solution, which is the most stable low-spin and insulating solution for the present parameter set, has been displayed. The shaded area shows the 3*d*-derived partial density of states. The 2*p* and 3*d* orbitals are strongly hybridized in the states just below and above the band gap, in good agreement with the cluster-model analysis. This indicates that the HF calculation correctly describes the character of the band gap. In the inset of Fig. 3.14, we have compared the experimental result with the density of states where the 2*p* and 3*d* partial density of states have been multiplied by their photoionization cross sections [Yeh and Lindau, 1985]. Here, the photoionization cross section of the O 2*p* subshell has also been multiplied by a factor three. According to the cluster model analysis, the peak at 1.5 eV of the experimental result is mainly from the $t_{2g}$ state where the Ni 3*d* and O 2*p* character are strongly hybridized. In the HF calculation, the $t_{2g}$ band is located at 2.5 eV and is shifted towards high binding energy by ~ 1 eV from the experimental result. The HF calculation also fails to reproduce the satellite structure.



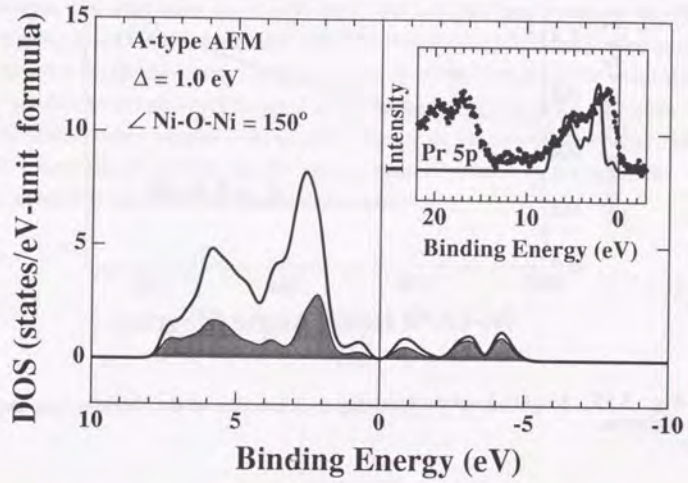


**Fig. 3.14.** Total density of states and the Ni 3*d* partial density of states (shaded region) for the *A*-type AFM state. The density of states obtained by multiplying the O 2*p* and Ni 3*d* partial density of states by their photoionization cross sections is compared with the experimental result in the inset.

In Fig. 3.15, we have plotted the magnitude of the band gap as a function of the Ni-O-Ni bond angle. The band gap increases as the $GdFeO_3$-type distortion becomes large for the *A*-type AFM solutions through the decrease in the intercluster Ni-O-Ni transfer integrals. This explains the observation that the increase of the $GdFeO_3$-type lattice distortion make $RNiO_3$ insulating [Lacorre *et al.*, 1992; Torrance *et al.*, 1992; García-Muñoz *et al.*, 1992a]. Barman, Chainani and Sarma [1994], on the other hand, attributed the origin of the metallic behavior of $LaNiO_3$ versus the insulating behavior of $NdNiO_3$ to the difference in the magnitude of the O 2*p*-to-Ni 3*d* transfer integral : Metallic $LaNiO_3$ has larger transfer integrals than insulating $NdNiO_3$. They also claimed that pressure causes an increase of the transfer integral and turns $NdNiO_3$ into metallic. Recently, a neutron diffraction study under pressure has been performed and has shown that the Ni-O-Ni bond angle and the Ni-O bond length change at the metal-insulator transition [Medarde *et al.*, 1995]. This result suggests that both the intra-cluster and intercluster changes are responsible for the metal-insulator transition.

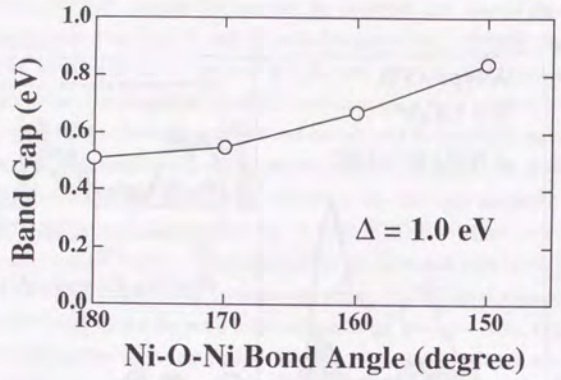


**Fig. 3.15.** Magnitude of the band gap as a function of the $GdFeO_3$-type lattice distortion.

### 3.5. Conclusion

By analyzing the photoemission spectra of $PrNiO_3$ using the cluster model, $\Delta$ is estimated to be ~ 1 eV. In the ground state, the $d^7$ configuration is strongly hybridized with the $d^8\underline{L}$ configuration. However, the local magnetic moment is calculated to be 0.9 $\mu_B$, which is close to the ionic value and is in good agreement with the neutron diffraction measurement [García-Muñoz *et al.*, 1992b]. The HF calculation using the parameters from the cluster-model analyses have shown that the $GdFeO_3$-type lattice distortion enlarges the magnitude of the band gap. The lattice distortion strongly affects the band gap of $PrNiO_3$, which has the small $\Delta$ and the covalent ground state.

In the present work, we have studied the electronic structure of $PrNiO_3$ by the two theoretical approaches: the local cluster calculation and the HF band-structure calculation. The comparison of the two extremes gives us a clue to understand how strongly correlation effect, especially the Heitler-London type effect, affects the metallic versus insulating behavior of $PrNiO_3$. On one hand, as shown in the previous section, HF calculations can give us a crude but useful picture of the metal-to-insulator boundary. The opening of band gaps for small, positive $\Delta$ has been discussed by Sarma [1990] in terms of the strong covalency in the ground state and has been called "covalent insulators". Following it, Nimkar *et al.* [1993] has studied



the metal-insulator boundary for the $CuO_2$ plane using the unrestricted HF approximation. The HF result, which does not include the Heitler-London type correlation effect, matches the view of "covalent" insulator. On the other hand, the local cluster approach, where the intra-cluster Heitler-London type correlation are exactly taken into account, can reproduce the various spectra, suggesting that electron correlation within the local cluster is important. Key questions are how strongly the Heitler-London type correlation is in the vicinity of the metal-insulator boundary and how far the picture of the local cluster model can survive in the real lattice. Since the HF calculation cannot reproduce the satellite structure of the valence-band photoemission spectra, it is necessary to see how the HF ground states is affected by the correlation effect when one attempts to reproduce the photoemission spectra.

# Chapter four

# Electronic structure of $LaCuO_3$ studied by photoemission and x-ray absorption spectroscopy

The electronic structure of the formally $Cu^{3+}$ metallic $LaCuO_3$ has been studied by photoemission and x-ray absorption spectroscopy. In the valence-band photoemission spectra, the intensity just below the Fermi level is very weak compared with the prediction of band-structure calculation and a charge-transfer satellite is observed. Such features are commonly observed in metallic Cu oxides including the high $T_c$ cuprates. By analyzing the valence-band and Cu 2*p* core-level photoemission spectra using a $CuO_6$ cluster model, the charge-transfer energy is estimated to be -1 eV, indicating that the ground state is dominated by the $d^9\underline{L}$ configuration with which the $d^8$ configuration is strongly hybridized. However, except for the satellite structure, agreement between the experimental results and the cluster-model calculations are not satisfactory. Especially, the Cu 2*p* x-ray absorption spectrum cannot be explained by the single-site cluster-model calculation, suggesting the importance of the intercluster interaction.

## 4.1. Introduction

Since the discovery of the high $T_c$ copper oxides [Bednorz and Müller, 1986], the electronic structure of the hole-doped $Cu^{2+}$ oxides has been subject to extensive investigations. X-ray absorption and photoemission studies on the high $T_c$ cuprates have revealed that the doped holes mainly go into the O 2*p* orbitals [Fujimori *et al.*, 1987; Shen *et al.*, 1987; Chen *et al.*, 1991]. Formally $Cu^{3+}$ oxides such as $NaCuO_2$ and $LaCuO_3$ have been frequently used as reference compounds in discussing the existence of $Cu^{3+}$ species in the high $T_c$ cuprates [Steiner *et al.*, 1987; Sarma *et al.*, 1988]. On the other hand, the electronic structure of the formally $Cu^{3+}$ oxides, which can be viewed as 100% hole-doped $Cu^{2+}$ oxides, has attracted interest because it remains to be clarified whether the ground states are dominated by $d^8$ (real $Cu^{3+}$) or $d^9\underline{L}$ (formally $Cu^{3+}$ but actually $Cu^{2+}$ plus an oxygen *p* hole $\underline{L}$). One of such compounds, $NaCuO_2$, has been studied by photoemission spectroscopy and cluster-model analysis and has been found to have a ground state of $d^9\underline{L}$ character with which $d^8$ character is heavily mixed [Mizokawa *et al.*, 1991; 1994]. In a compound with this type of ground state, the magnitude of the band gap is determined by the relative strength of the hybridization within the local $CuO_n$ cluster and that between the clusters. $NaCuO_2$, which has a 90° Cu-O-Cu bond angle, is insulating because the band gap opens due to the strong Cu 3*d*-O 2*p* hybridization within the $CuO_4$ cluster and the intercluster interaction is weak. On the other hand, in $LaCuO_3$ with a perovskite-type structure, which has an almost 180° Cu-O-Cu bond angle, the intercluster interaction is expected to be strong.

For $LaCuO_3$, two types of crystal structures have been reported: a rhombohedrally-distorted perovskite structure synthesized at higher oxygen pressure [Demazeau *et al.*, 1972] and a tetragonally-distorted perovskite structure synthesized at lower oxygen pressure [Bringley *et al.*, 1990]. Both the rhombohedral and tetragonal $LaCuO_3$ have been found to be poor metal [Demazeau *et al.*, 1972; Bringley *et al.*, 1993]. It has also been reported that the stoichiometric tetragonal $LaCuO_3$ shows a semiconducting behavior [Darracq *et al.*, 1993]. Band structure calculations using the local-density approximation (LDA) predict $LaCuO_3$ to be a Pauli-paramagnetic metal [Takegahara, 1987; Czyzyk and Sawatzky, 1994; Hamada *et al.*, 1995]. Based on the LDA+U calculation, which predict $LaCuO_3$ to be an antiferromagnetic (AFM) insulator, Czyzyk and Sawatzky [1994] have claimed that the tetragonal $LaCuO_3$ is a semiconductor for the ideal stoichiometry and that its metallic behavior is derived from the oxygen deficiency. Few high energy spectroscopic experiments such as photoemission spectroscopy, which provide important information on the electronic structure, have been reported and the electronic structure of $LaCuO_3$ remains controversial. In this chapter, we are going to present photoemission and x-ray absorption spectra of the tetragonal $LaCuO_3$ and results of the configuration-interaction (CI) cluster-model analysis. We have also performed unrestricted Hartree-Fock (HF) calculation and subsequent self-energy correction calculations on a Cu 3*d*-O 2*p* lattice model using the electronic-structure parameters obtained from the cluster-model analyses.



## 4.2. Experimental

Polycrystalline samples of $LaCuO_3$ were supplied by Prof. Takeda's group in Mie University. A mixture of $La_2O_3$ and CuO was pressed into a pellet and fired at 850°C for 2-3 hours in air. The product was milled and pressed into a pellet again. After firing at 1000°C in air for 24 hours, $LaCuO_{2.5}$ was obtained. The sample was further fired at 800°C and 200 atom for 48 hours and at 400°C and 400-500 atom for 3-4 days in an $O_2$ gas flow. Stoichiometry of the compounds was established by iodometric titration.

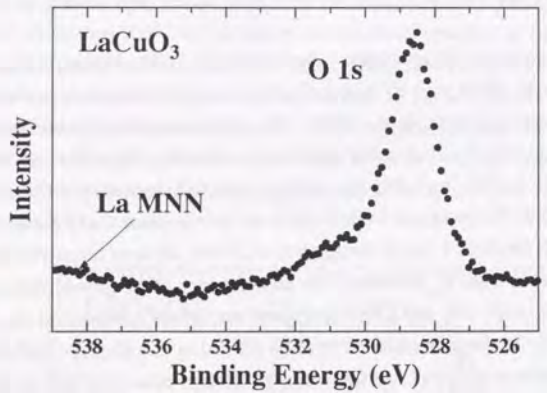


**Fig. 4.1.** O 1*s* XPS spectrum of $LaCuO_3$.

A Mg Kα source ($h\nu$=1253.6 eV) was used for x-ray photoemission spectroscopy (XPS). The XPS spectra were corrected for the Mg $K\alpha_{3,4}$ ghost. A He discharge lamp ($h\nu$=21.2 eV for He I and 40.8 eV for He II) were used for ultraviolet photoemission spectroscopy (UPS). Photoelectrons were collected with a PHI double-pass cylindrical-mirror analyzer. The resolution including both the source width and the instrumental broadening was about 1.0 eV, 0.35 eV and 0.25 eV for XPS, He II and He I, respectively. UPS spectra were also measured at beamline BL-2 of Synchrotron Radiation Laboratory, Institute for Solid State Physics, University of Tokyo. The energy resolution was 0.3-0.5 eV for photon energies ranging from 40 to 100 eV. The Fermi level was determined by evaporating Au on the sample. The binding energy in XPS was calibrated using the Au $4f_{7/2}$ peak at 84.0 eV [Hüfner, 1995]. In order to prevent possible loss of oxygens from the surface, the samples were cooled to

liquid-nitrogen temperature (LNT) during the measurements. X-ray absorption spectroscopy (XAS) was done at beamline BL-2B of Photon Factory, Laboratory for High Energy Physics. The energy resolution was ~ 0.2 eV at 530 eV. The photon energy was calibrated using the O 1s edge of $TiO_2$ at 530.7 eV [Abbate *et al.*, 1992] and the Cu $2p_{3/2}$ edge of Cu metal at 932.5 eV [Grioni *et al.*, 1989]. The XAS spectra was taken at room temperature (RT) in the total electron yield method. In order to obtain fresh, clean surfaces, the samples were scraped in situ with a diamond file. The O 1s core-level spectrum became a single peak by scraping both at RT and at LNT (Fig. 4.1), indicating good sample quality. The base pressure in the spectrometer was in the low $10^{-10}$-torr range for XPS and UPS and was ~ $1\times10^{-9}$ torr for XAS.

## 4.3. Results and Discussion

### 4.3.1. Core-level XPS

The Cu 2*p* core-level XPS spectrum is shown in Fig. 4.2. The binding energy of the Cu $2p_{3/2}$ peak is 934.5 eV, which is ~1 eV higher than that of CuO and is ~ 2 eV higher than those of $Cu_2O$ and Cu metal [Ghijsen *et al.*, 1988]. The Cu 2*p* spectrum has satellite structures, which have been generally observed in late transition-metal oxides. Therefore, we have applied the CI cluster-model analysis including the multiplet effect [Zaanen *et al.*, 1986; Okada and Kotani, 1991]. Since in the tetragonal $LaCuO_3$ there are four in-plane Cu-O bonds of 1.909 Å and two apical Cu-O bonds of 1.986 Å [Bringley *et al.*, 1993], we have employed an elongated octahedral $CuO_6$ cluster with $D_{4h}$ symmetry. The wave function of the ground state is given by a linear combination of $d^8$, $d^9\underline{L}$ and $d^{10}\underline{L}^2$ configurations, where $\underline{L}$ represents an oxygen 2*p* hole. The O 2*p*-to-Cu 3*d* charge-transfer energy $\Delta$ is defined by $\Delta \equiv E(d^9\underline{L}) - E(d^8)$ and the 3*d*-3*d* Coulomb interaction energy by $U \equiv E(d^9) + E(d^7) - 2E(d^8)$, where $E(d^n\underline{L}^m)$ is the center of gravity of the $d^n\underline{L}^m$ multiplet. The transfer integrals between the Cu 3*d* and O 2*p* orbitals are expressed in terms of Slater-Koster parameters $(pd\sigma)$ and $(pd\pi)$ [Slater and Koster, 1954]. The ratio $(pd\sigma)/(pd\pi)$ is fixed at ~ -2.2 [Mattheiss, 1972; Harrison, 1989]. The transfer integrals between the O 2*p* orbitals are given by $(pp\sigma)$ and $(pp\pi)$, which are fixed at 0.60 and -0.15 eV respectively. In addition, we have scaled the transfer integrals following Harrison's rule [Harrison, 1989]. The value of $(pd\sigma)$ given below is for the in-plane Cu-O bond. The multiplet coupling between the 3*d* electrons is included through Racah parameters *B* and *C*, which are fixed at 0.150 and 0.667 eV, namely, ~ 80% of the atomic HF values [Mann; de Groot *et al.*, 1990; Okada and Kotani, 1991]. The wave functions of the final states are given by linear combinations of $\underline{c}d^8$, $\underline{c}d^9\underline{L}$ and $\underline{c}d^{10}\underline{L}^2$ configurations, where $\underline{c}$ denotes a Cu 2*p* core hole. The multiplet coupling between the Cu 2*p* core hole and Cu 3*d* electrons is expressed in terms of Slater integrals $F^2$, $G^1$ and $G^3$, which are also fixed to 7.08, 5.37 and 3.06 eV, namely, ~ 80% of the atomic HF values [Mann; de Groot *et al.*, 1990; Okada and Kotani, 1991]. In the cluster-model analysis of the Cu 2*p* XPS, we have four adjustable parameters: $\Delta$, $U$, $(pd\sigma)$ and the multiplet-averaged 2*p*-3*d* Coulomb interaction $Q$ $[\equiv F^0 - (1/15)G^1 - (3/70)G^3]$.



Here, we have fixed $U$ and $Q$ at 7.0 eV and 9.0 eV, respectively, which are close to the values obtained commonly in the cluster-model analyses of the late transition-metal oxides [Okada and Kotani, 1991; Bocquet *et al.*, 1992b]. The best fit is obtained for $\Delta = -1.0 \pm 1.0$ eV and $(pd\sigma) = -1.7 \pm 0.2$ eV as shown in Fig. 4.2. The ground state is the high-spin state with ${}^3B_{1g}$ symmetry because the elongation of the octahedra or the ratio of the apical Cu-O bond length to the in-plane one ~ 1.04 is too small. In order to stabilize the low-spin state compared with the high-spin state, the ratio is required to be lager than 1.13 with the best-fit parameter set. The ground state has 37% $d^8$, 53 % $d^9\underline{L}$ and 10% $d^{10}\underline{L}^2$ characters. The final states are decomposed into the $\underline{c}d^8$, $\underline{c}d^9\underline{L}$ and $\underline{c}d^{10}\underline{L}^2$ components in the lower panel of Fig. 4.2. The main peaks have both $\underline{c}d^{10}\underline{L}^2$ and $\underline{c}d^9\underline{L}$ character and the satellite structures have $\underline{c}d^9\underline{L}$ character. In the ground state, the net number of the 3*d* holes is 1.27, which is close to the ionic value of $Cu^{2+}$ rather than $Cu^{3+}$. In this sense, the electronic structure of $LaCuO_3$ given by the single-site cluster model is similar to that of $NaCuO_2$ [Mizokawa *et al.*, 1991; 1994]. However, it is expected that the intercluster interaction is important in $LaCuO_3$ which has an almost 180° Cu-O-Cu bond. Actually, the asymmetric line shape of the main peak cannot be explained by the cluster-model calculation, which may be due to the intercluster interaction beyond the single-site cluster model [van Veenendaal and Sawatzky, 1994].

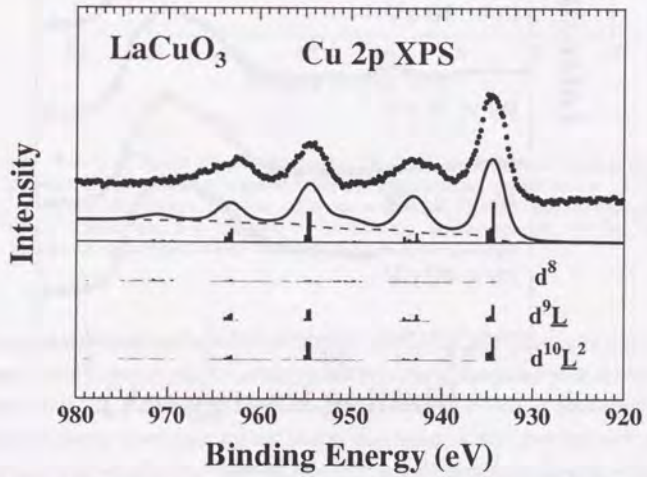


**Fig. 4.2.** Cu 2*p* core-level spectrum of $LaCuO_3$ compared with the CI cluster model calculation (upper panel). Decomposition of the line spectra into final-state configurations is shown in the lower panel.

### 4.3.2. Valence band

The valence-band photoemission spectra taken at various photon energies from 40 eV to 1253.6 eV are displayed in Fig. 4.3. Since the relative photoionization cross section of O 2*p* to Cu 3*d* increases as the photon energy decreases, the structures at 3 and 5 eV mainly have the O 2*p* and Cu 3*d* characters, respectively. In the UPS spectrum taken at $h\nu$ = 90 eV, the existence of the satellite structure located at ~ 12 eV is clear. The satellite region from 9 eV to 13 eV is strongly enhanced and the main-band region from 0 eV to 7 eV is not enhanced by the 3*p*-3*d* resonance ($h\nu$ = 74 eV: on resonance, $h\nu$ = 70 eV: off resonance), indicating that the satellite can be regarded as a so-called charge-transfer satellite.

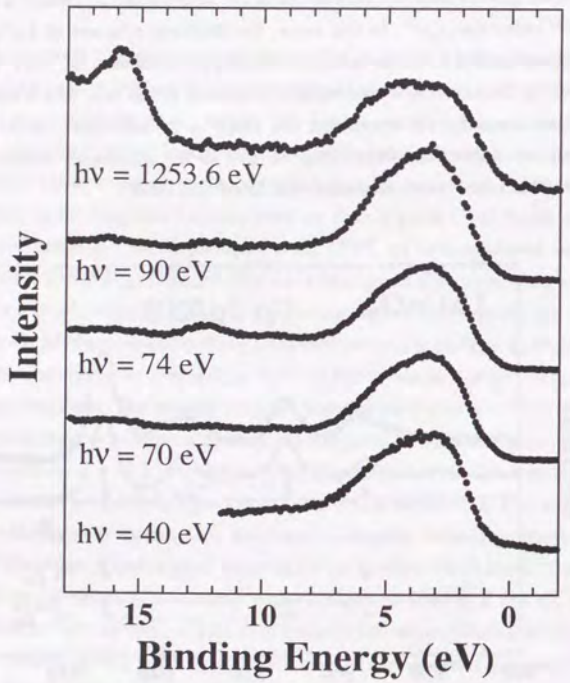


**Fig. 4.3.** Valence-band photoemission spectra of $LaCuO_3$ taken at $h\nu$ = 40, 70, 74, 90, 1253.6 eV.



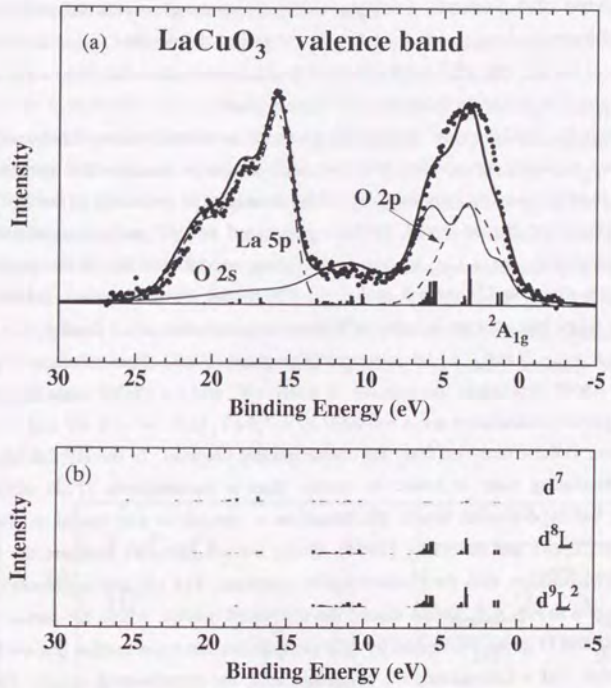


**Fig. 4.4.** (a) Cluster-model calculation (thick solid curve) for valence-band photoemission spectra compared with the experimental result ($h\nu$ = 1253.6 eV) of $LaCuO_3$ (dots). The thin solid curve indicate the contribution from the Cu 3*d* orbitals which is obtained by broadening the line spectra. (b) The line spectra are decomposed into the configurational components.

The calculated line spectra with $\Delta$ = -1.0 eV, $U$ = 7.0 eV and ($pd\sigma$) = -1.7 eV have been broadened with a Gaussian and a Lorentzian and have been compared with the valence-band XPS spectrum in Fig. 4.4. The full width at half maximum (FWHM) of the Gaussian is ~ 1.0 eV, which is mainly determined by the energy resolution of the analyzer, and that of the Lorentzian is ~ 0.4 + 0.3$E_B$ eV, where the first term is derived from the natural width of the x-ray source and the second term proportional to the binding energy $E_B$ is from the life time of the final states. The satellite structure, whose existence becomes clear by subtracting the background due to secondary electrons, is well reproduced. Here, we have added the

contribution from the O 2*p* band of a Gaussian form centered at ~ 3 eV whose relative cross section to the Cu 3*d* band is assumed to be three time larger than that of the atomic calculation [Yeh and Lindau, 1985; Sawatzky and Post, 1979]. From the cluster-model analysis, the final states both of the main-band region from 0 to 8 eV and of the satellite region from 8 to 13 eV are mixtures of the $d^8\underline{L}$ and $d^9\underline{L}^2$ configurations. The first ionization state has $^2A_{1g}$ symmetry, which is obtained by emission from the $x^2$-$y^2$-type orbitals.

Although the cluster-model calculation gives us an overall picture of the valence-band XPS spectrum including the satellite structure, it is unable to describe the structure near the Fermi level. In order to investigate the effect of the translational symmetry of the Cu 3*d* orbitals beyond the single-site cluster model, we have performed the HF and subsequent self-energy correction calculations on a Cu 3*d* and O 2*p* lattice model. Details of the method of the calculations are given in Chapters 5 and 6. In this model, the intra-atomic 3*d*-3*d* Coulomb interaction is taken into account in terms of Kanamori parameters, $u$, $u'$, $j$ and $j'$, for which the relationships $u' = u - 2j$ and $j' = j$ are assumed [Kanamori, 1963]. These Kanamori parameters are related to Racah parameters through $u = A + 4B + 3C$ and $j = (5/2)B + C$. The parameters used for the present calculation are $\Delta = 0.0$ eV, $U = 7.5$ eV, $(pd\sigma) = -1.8$ eV and $j = 0.92$ eV, which are close to those obtained from the cluster-model analyses. In the HF calculation, a *G*-type AFM insulating state is lower in energy than a paramagnetic (PM) metallic state, contradicting the experimental result. The situation is similar to that found in the LDA+U calculation by Czyzyk and Sawatzky [1994]. Here, we are going to compare the density of states of the PM solution with the photoemission spectrum. The HF and self-energy corrected results are shown in Fig. 4.5. In the insets, the calculated results, where the partial density of states of Cu 3*d* and O 2*p* are multiplied by their photoionization cross section and are broadened with a Gaussian and a Lorentzian, are compared with the experimental results. For the HF result, the FWHM's of the Gaussian and Lorentzian are the same as those for the cluster-model calculation. For the self-energy corrected result, the FWHM of the Lorentzian can be fixed at 0.4 eV. The HF solution for the PM metal is essentially the same as that of the LDA calculation [Takegahara, 1987; Czyzyk and Sawatzky, 1994; Hamada *et al.*, 1995]. In the HF calculation, the broad $e_g$ band, in which the O 2*p* and Cu 3*d* orbitals are strongly hybridized, crosses the Fermi level. As a result, the calculated $t_{2g}$ band is located at ~ 3 eV, which is too deep, and the deviation from the experimental result is very large. The HF calculation also fails to reproduce the satellite structure from 8 to 13 eV. In order to calculate the self-energy around the HF solution, we have performed the second order perturbation expansion in Coulomb interaction using the local approximation, namely, neglecting the momentum dependence of the self-energy. In the self-energy corrected result, the broad $e_g$ band is strongly renormalized and is narrowed and part of the spectral weight is transferred to the satellite region. However, the band narrowing and the intensity of the satellite structure are too strong, indicating the excessive self-energy correction. In the metallic solution, the screening effect may be important



and may have to be taken into account, *e. g.*, through the random phase approximation (RPA). Inclusion of higher-order RPA-type diagrams is expected to weaken the self-energy correction and improve the agreement with the experimental result.

The intensity just below the Fermi level, which is overestimated in the HF calculation, is still too strong in the self-energy corrected spectral function compared with the experimental result. In order to reproduce the intensity at the Fermi level using the self-energy calculation, strong momentum dependence of the self-energy is required. When the momentum dependence of the self-energy is strong and $m_k/m_{HF}$ is much lower than 1, the spectral weight at the Fermi level is multiplied by the factor $m_k/m_{HF}$ and is strongly reduced. Here, $m_{HF}$ is the band mass in the HF calculation and $m_k/m_{HF}$ is defined by (2.55). In three dimensional systems, the momentum dependence of the self-energy beyond the local approximation is not so strong as long as the interaction is restricted on the same site [Schweitzer and Czycholl, 1990]. Therefore, it is natural to consider that the insufficiency of the momentum dependence of the self-energy would not be due to the local approximation but would probably be due to the deficit of the present model.

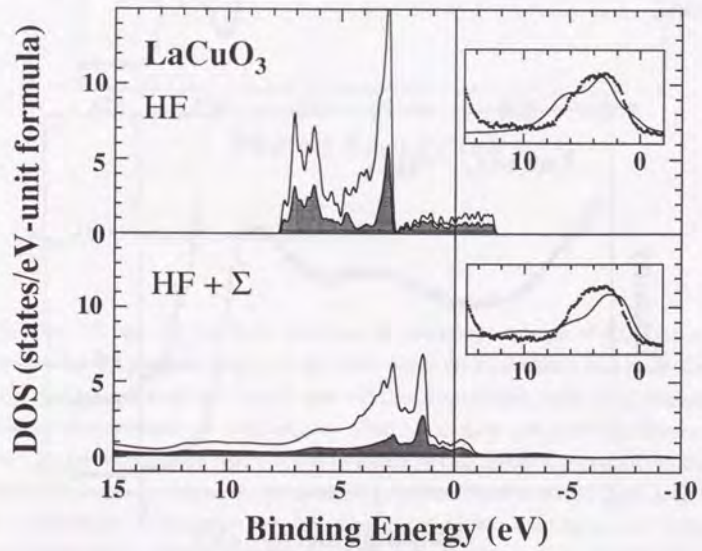


**Fig. 4.5.** Spectral function of $LaCuO_3$ calculated using the HF approximation (upper panel) and that including the self-energy correction calculated using the second-order perturbation (lower panel). The shaded area indicates the transition-metal 3*d* spectral weight. In the insets, the calculated results are compared with the valence-band XPS spectrum.

In Fig. 4.6, we have plotted the valence-band photoemission spectrum taken at $h\nu$ = 21.2 eV. Small but finite spectral weight is observed at the Fermi level, which is consistent with the fact that $LaCuO_3$ is metallic. Our samples have been synthesized by taking care of the stoichiometry. The spectra have been taken within 10 minuets after scraping at low temperature. Therefore, the oxygen loss in the bulk before the measurement and that from the surface during the measurement was avoided as much as we could. At least, this measurement indicates that almost stoichiometric $LaCuO_3$ has a small but finite spectral weight at the Fermi level. It should be noted that the spectral weight at the Fermi level in the experimental results is also very small in the UPS spectra compared with the calculated results which is shown in Fig. 4.5. Such a feature has commonly been observed in the UPS spectra of other PM metallic transition-metal oxides such as $LaNiO_3$ [Kemp and Cox, 1990], $Ca_{1-x}Sr_xVO_3$ [Fujimori *et al.*, 1992a; Eisaki, 1992; Inoue *et al.*, 1995; Morikawa *et al.*, 1995] and $La_{1-x}Sr_xTiO_3$ [Fujimori *et al.*, 1992b]. Because the Hubbard model or the Anderson lattice model with on-site Coulomb interaction will not lead to such a strong momentum dependence in the self-energy, the effects of long-range Coulomb interaction or electron-phonon interaction, etc., which are not included in the present model, would be necessary to explain the observed reduction. A possible explanation will be discussed in Chapter 6, where the effect of the inter-site Coulomb interaction is investigated.

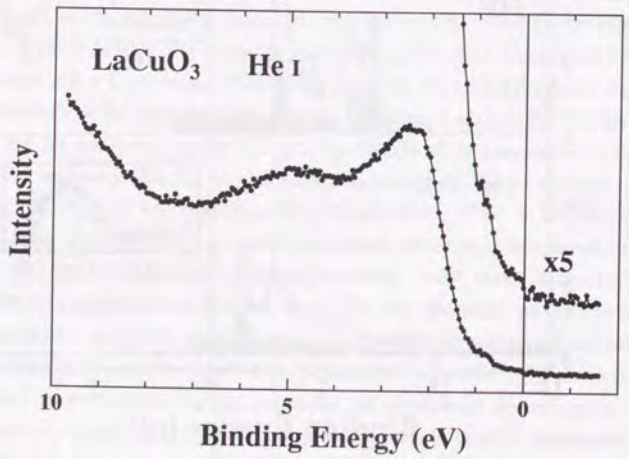


**Fig. 4.6.** Valence-band photoemission spectra of $LaCuO_3$ taken at $h\nu$ = 21.2 eV.



### 4.3.3. X-ray absorption spectra

The O 1*s* XAS spectrum of $LaCuO_3$ is shown in Fig. 4.7. The peak at ~ 528 eV is mainly derived from the O 2*p* weight hybridized into the unoccupied Cu $e_g$ state. If $LaCuO_3$ is viewed as a 100% hole-doped $Cu^{2+}$ oxide, the peak corresponds to that growing with the hole doping in the pre-edge region of $La_{2-x}Sr_xCuO_4$ [Chen *et al.*, 1991]. The structures ranging from 530 eV to 545 eV are due to the La 4*f*, 5*d* and Cu 4*s*, 4*p* states.

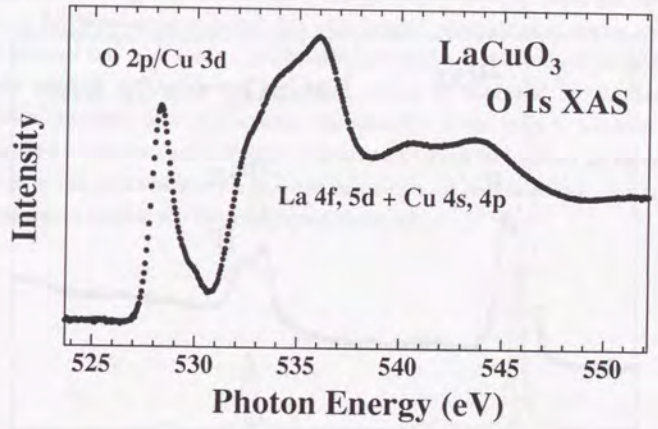


**Fig. 4.7.** O 1*s* XAS spectrum of $LaCuO_3$.

In Fig. 4.8, the Cu 2*p* XAS spectrum is compared with the $CuO_6$ cluster-model calculation using the parameter set for Cu 2*p* XPS. From the local-cluster viewpoint, the $2p_{3/2}$ and $2p_{1/2}$ main peaks located at ~ 931 eV and ~ 951 eV, respectively, have $\underline{c}d^{10}\underline{L}$ character and the broad satellite structures at ~ 940 eV and ~ 960 eV to have $\underline{c}d^9$ character. However, the $2p_{3/2}$ and $2p_{1/2}$ main peaks are split into two structures, which makes it impossible to fit the Cu 2*p* XAS by the single-site cluster-model calculation. Let us denote these structures as A, A', B, and B', respectively, as shown in Fig. 4.8. Sarma *et al.* [1988] and Chen *et al.* [1992] have observed that the new structure, which is located at ~ 2 eV higher energy than the main peak, grows as an insulating $Cu^{2+}$ oxide is hole-doped. Van Veenendaal and Sawatzky [1994] have calculated the Cu 2*p* XAS for 50% doped $Cu^{2+}$ oxide using a two-site cluster model and have shown that a new structure, in which the intercluster screening effect is weak, appears on the

high energy side of the main structure, in which the intercluster screening effect is strong. Therefore, it is natural to consider that structures A and A' are derived from the states strongly screened by intercluster interaction and structures B and B' from those weakly screened. The Cu 2*p* XAS spectrum suggests that the intercluster interaction is very strong in $LaCuO_3$, which has a 180° Cu-O-Cu bond angle. When the intercluster interaction is weak, the splitting between A (A') and B (B') is expected to disappear [van Veenendaal and Sawatzky, 1994]. Actually, in $NaCuO_2$ which has a 90° Cu-O-Cu bond angle, the Cu $2p_{3/2}$ and $2p_{1/2}$ main peaks are almost single peaks [Sarma *et al.*, 1988].

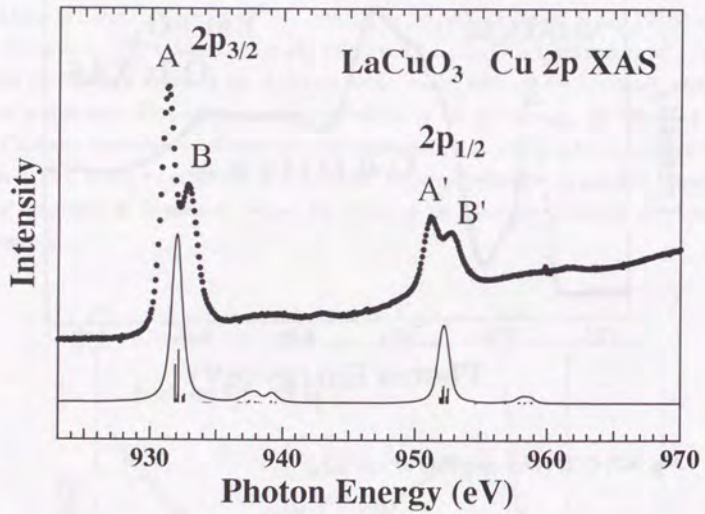


**Fig. 4.8.** Cu 2*p* XAS spectrum of $LaCuO_3$ (dots) compared with the cluster-model calculation (solid curve).

## 4.4. Conclusion

We have investigated the electronic structure of $LaCuO_3$ by means of photoemission and x-ray absorption spectroscopy. The charge-transfer satellite observed in the valence-band and Cu 2*p* core-level photoemission spectra allow us to apply the CI cluster-model analyses to $LaCuO_3$. From the analyses, the charge-transfer energy is estimated to be ~ -1 eV and the



ground state mainly has $d^9\underline{L}$ character although in the ground state the $d^8$ configuration is strongly hybridized into the $d^9\underline{L}$ configuration. The Cu 2*p* XAS spectrum, which cannot be explained by the single-site cluster-model calculation, shows the importance of the intercluster interaction in $LaCuO_3$. These experimental results and analyses naturally lead us to the conclusion that $LaCuO_3$, which has an almost 180° Cu-O-Cu bond angle, is made metallic by the strong intercluster interaction while $NaCuO_2$, which has a 90° Cu-O-Cu bond angle, is insulating because of the weak intercluster interaction. In order to fully understand the XPS and XAS spectra of $LaCuO_3$, we have to include the intercluster interaction.

We have also performed the HF and subsequent self-energy calculations on the Cu 3*d*-O 2*p* lattice models using the electronic-structure parameters obtained from the cluster-model analysis of the photoemission spectra. The valence-band photoemission spectra including the satellite structure is to some extent reproduced but the weak spectral intensity at the Fermi level compared with the band-structure calculation cannot be explained by the second-order perturbation calculation of the self-energy. The reduction of the spectral weight at the Fermi level may be due to the unusual correlation effect which cannot be obtained by the perturbation calculation or due to interaction which is not included in the present model such as the long-rang Coulomb interaction and electron-phonon interaction.